

Universidade Federal de Juiz de Fora
Faculdade de Engenharia
Programa de Pós-Graduação em Engenharia Elétrica

Dayane Oliveira Gonçalves

**Fast Online Filtering Based on Data Fusion of Two Highly Segmented
Detectors**

Juiz de Fora
2017

Ficha catalográfica elaborada através do Modelo Latex do CDC da UFJF
com os dados fornecidos pelo(a) autor(a)

Oliveira Gonçalves, Dayane.

Fast Online Filtering Based on Data Fusion of Two Highly Segmented
Detectors / Dayane Oliveira Gonçalves. – 2017.

69 f. : il.

Orientadores: Augusto Santiago Cerqueira

Luciano Manhães de Andrade Filho

Dissertação (Mestrado) – Universidade Federal de Juiz de Fora, Faculdade
de Engenharia. Programa de Pós-Graduação em Engenharia Elétrica, 2017.

1. Detecção de sinal.
2. Filtro casado.
3. Processamento digital de sinal.
4. Física de partículas I. Santiago Cerqueira, Augusto, orient. II. Manhães
de Andrade Filho, Luciano, orient. Título.

Dayane Oliveira Gonçalves

**Fast Online Filtering Based on Data Fusion of Two Highly Segmented
Detectors**

Dissertação apresentada ao Programa de Pós-Graduação em Engenharia Elétrica da Universidade Federal de Juiz de Fora, na área de concentração em Sistemas Eletrônicos , como requisito parcial para obtenção do título de Mestre em Engenharia Elétrica.

Orientadores: Augusto Santiago Cerqueira
Luciano Manhães de Andrade Filho

Juiz de Fora

2017

Dayane Oliveira Gonçalves

Fast Online Filtering Based on Data Fusion of Two Highly Segmented Detectors

Dissertação apresentada ao Programa de Pós-Graduação em Engenharia Elétrica da Universidade Federal de Juiz de Fora, na área de concentração em Sistemas Eletrônicos , como requisito parcial para obtenção do título de Mestre em Engenharia Elétrica.

Aprovada em 11 de abril de 2017

BANCA EXAMINADORA

Prof. Dr. Augusto Santiago Cerqueira - Orientador
Universidade Federal de Juiz de Fora

Prof. Dr. Luciano Manhães de Andrade Filho -
Orientador
Universidade Federal de Juiz de Fora

Professor Dr. José Manoel de Seixas
Universidade Federal do Rio de Janeiro

Professor Dr. Rafael Antunes Nóbrega
Universidade Federal de Juiz de Fora

Dedico esta dissertação aos meus pais, Sérgio e Eliete

AGRADECIMENTOS

Mais uma etapa que se encerra e, com ela, a certeza de que não teria chegado até aqui sozinha. Agradeço a Deus por todas as oportunidades, aprendizados e pessoas que cruzaram meu caminho durante o mestrado.

Ao Augusto, me faltam palavras para agradecer por todos os ensinamentos, disponibilidade, conselhos durante esses últimos 4 anos da minha vida acadêmica. Você é um ótimo orientador, sinto que aprendi muito e me tornei uma engenheira melhor sob sua orientação. Ao prof. Luciano, por me ensinar os caminhos das pedras quando cheguei ao CERN, pela orientação e sugestões sobre este trabalho, muito obrigada. Ao prof. Seixas, muito obrigada por toda paciência e conselhos que foram fundamentais para meu crescimento acadêmico e profissional. Ainda, aos três, meu eterno obrigada pela confiança e oportunidade de concluir metade do meu mestrado no CERN e pelo presente que foi o projeto TileMuon, de certo essa experiência mudou a minha vida e minha forma de ver o mundo. Ao prof. Bernardo, muito obrigada por compartilhar seus conhecimentos e por toda ajuda durante esses anos de convivência.

Ao meu pai Sérgio, por abraçar todas as minhas escolhas como se fosse sua, por me ensinar as minhas primeiras lições sobre eletrônica bem como a paixão por ela, por ser meu exemplo, meu melhor amigo, e, acima de tudo, por ser amor. A minha mãe Eliete, por me ensinar, com seu exemplo, a ser uma mulher forte, a ter garra para lutar pelos meus sonhos, por nossas longas conversas, principalmente durante o intercâmbio, que muitas vezes eram a melhor parte do meu dia e por todas as suas orações e pensamentos. Ao meu irmão Luiz, obrigada pela amizade e todas as experiências compartilhadas durante esses anos. Amo vocês! A toda a minha família, pelos momentos compartilhados, por tornarem minha vida mais leve e mais feliz!

A minha amiga Flávia, obrigada pela sua generosidade em compartilhar comigo seus conhecimentos acadêmicos durante este trabalho, e, principalmente, por tornar minha experiência durante o intercâmbio melhor. Meu eterno obrigada por ser amiga, confidente, companheira e família nos momentos em que eu mais precisei. Ao amigos que fiz em Genebra, Gabi, Natalia, Livio, Jake, Bruno, Leandro, Bárbara, Ian, Lucas, Claire e Héron, obrigada pelos bons momentos compartilhados, pelos almoços e coversas. Aos meus amigos de sempre, Laís, Karina, Natália, Verônica, Igor, Thiago e Elisa, muito obrigada por todo o companherismo e cumplicidade durante todos esses anos.

For fim, obrigada a todos os meus professores e todos que contribuiram de alguma forma para o meu crescimento acadêmico e pessoal durante toda esta caminhada.

“Only one who devotes himself to a cause with his whole strength and soul can be a true master. For this reason mastery demands all of a person.”
(Albert Einstein)

RESUMO

O calorímetro de Telhas (TileCal) é o calorímetro hadrônico central de um dos experimentos do Grande Colisor de Hádrons (LHC), o ATLAS. O TileCal fornece medidas de energia finamente segmentadas (10.000 canais de leitura) para as partículas incidentes no detector. Análises realizadas nos dados resultantes de colisões de partículas constataram que utilizar as informações da camada radial externa do TileCal, em coincidência com as câmaras de múons (MS) do ATLAS, pode proporcionar uma redução de falsos sinais de trigger (filtragem online) de múons gerados pelas iteração de prótons de baixo momento, na blindagem do feixe do LHC, com o MS. O projeto TileMuon foi desenvolvido para este propósito e sua principal atividade, no programa de atualização ATLAS, é habilitar o TileCal para fornecer as informações de trigger para a primeira etapa de filtragem online para a identificação de múons no ATLAS. Esta dissertação apresenta o estudo, o desenvolvimento e a implementação de uma técnica para a identificação de múons no contexto TileMuon. Técnicas de estimativa encontradas na literatura foram aplicadas no contexto do projeto e comparadas. Os resultados para dados experimentais mostraram que o método para a identificação de múons, baseado no filtro casado para ruído gaussiano, obteve o melhor desempenho, em termos de erro de detecção, bem como viabilidade de implementação online, e foi a técnica escolhida para a aplicação.

Palavras-chave: Identificação de Múons. Filtro casado. Processamento digital de sinal. Física de partículas.

ABSTRACT

The Tile Calorimeter (TileCal) is the central hadronic calorimeter of the ATLAS experiment at the Large Hadron Collider (LHC). TileCal provides highly-segmented energy measurements for incident particles. Information from TileCal's outermost radial layer in coincidence with the ATLAS muon chambers can provide a reduction of the fake muon triggers due to slow charged particles (typically protons). The TileMuon project was development aims this purpose and its main activity of the Tile-Muon Trigger in the ATLAS upgrade program is to install and to activate the TileCal signal processor module for providing trigger inputs to the Level-1 Muon Trigger. This dissertation presents the study, the development and the implementation of the Muon identification technique in the TileMuon context. Amplitude estimation techniques found in the literature were applied to the problem and confronted against each other. The results for experimental data shown that the Muon identification based on the maximum likelihood for Gaussian noise achieved the best performance in terms of detection error as well as online implementation feasibility, and it has been the chosen technique for the application.

Key-words: Muon identification, Matched Filter, Digital Signal Processing, High Energy Physics.

LIST OF FIGURES

Figure 1 – CERN’s Accelerator complex (Extracted from [4]).	20
Figure 2 – Overall view of the LHC experiments (Extracted from [5]).	21
Figure 3 – Basic Structure of the ATLAS experiment (Extracted from [14]).	22
Figure 4 – ATLAS coordinate system.	23
Figure 5 – Transverse view of the ATLAS, showing the detection strategy (Extracted from [15]).	23
Figure 6 – A computer generated image of the full calorimeter (Extracted from [15]).	25
Figure 7 – Segmentation of the EM calorimeter of ATLAS.((Extracted from [19]) .	26
Figure 8 – The Tile calorimeter design principle (Extracted from [14]).	27
Figure 9 – The calorimeter segmentation for one module of the barrel ($\eta > 0$) and one module of the extended barrel (Extracted from [21]).	28
Figure 10 – TileCal Readout Signal Chain (Extracted from [22]).	29
Figure 11 – Schematic overview of the Trigger and DAQ system (Extracted from [26]).	30
Figure 12 – Illustration of the coincidence between TileCal extended barrel and the end-cap muon chamber (Extracted from [21]).	31
Figure 13 – Distribution of Level-1 muons as a function of η and for a p_T threshold of 20 GeV. The combined yellow (shaded) and white (un-shaded) distribution is with the NSW included in the Level-1 muon endcap decision. The yellow (shaded) distribution alone shows the effect of including the outer layer of the TileCal extended barrel in the Level-1 muon endcap decision. (The underlying cyan (dark-shaded) distribution represents offline reconstructed muons after an offline 25 GeV pT cut). Extracted from [28]).	32
Figure 14 – Muon detection efficiency and Level-1 muons rate reduction as a function of TileCal cell energy sum threshold. False alarm values are also shown, giving the probability that in each bunch crossing the sum of the energies deposited in D5 and D6 will be over threshold. Results were obtained using standard offline readout data. A smearing of 200 MeV was introduced in the response of each cell to simulate the electronics noise of the Level-1 readout. Extracted from [28].	33
Figure 15 – Muon detection efficiency and rate reduction as a function of TileCal cell energy sum threshold. Extracted from [22].	34
Figure 16 – TileMuon System basic architecture.	35
Figure 17 – TMDB Design.	35
Figure 18 – A typical unipolar pulse shape of a calorimeter whose digital samples are extracted from signal.	40
Figure 19 – The LAr ionization Pulse Shape (Extracted from [44]).	42
Figure 20 – Typical pulse shape measured in CMS (Extracted from [45])	43

Figure 21 – Signal reconstruction procedure using the Matched Filter(Extracted from [46]).	46
Figure 22 – The Matched Filter implementation for N=7.	47
Figure 23 – The TMDB hardware system: (a) the TileMuon digitalizer board. (b) the TMDB crate.	48
Figure 24 – The noise distribution of channels from TileCal module EBA02.	49
Figure 25 – The noise covariance matrix of channels from TileCal module EBA01. .	50
Figure 26 – Noise cross correlation between (a) all the channels of A side (b) Channels of one TMDB of A side (c) all the channels of C side (d) Channels of one TMDB of C side.	51
Figure 27 – Reference pulse acquired to both A and C Tilecal's side.	52
Figure 28 – The pulse shape for different charges.	53
Figure 29 – The pulse shape from different proton-proton collisions datasets for (a) channel D5L of TileCal module EBA01 (b)channel D5L of TileCal module EBAC01.	53
Figure 30 – The matched filter weights for channels from TileCal module EBC01. .	54
Figure 31 – The TMDB calibration output estimated by Matched Filter (arbitrary units) for TileCal module EBC03 channel D5L to convert the value to MeV.	55
Figure 32 – The error estimation distribution for TileCal module EBC03 channel D5L.	55
Figure 33 – Correlation between the on-line TMDB output (using the variable eTMDB) and the off-line operation.	56
Figure 34 – TMDB electronic noise channel map acquired during the pedestal run in 2016.	57
Figure 35 – Muon detection efficiency and fake reduction of the Level-1 Tile-Muon Trigger as a function of TileCal cell energy sum threshold.	59
Figure 36 – Muon detection efficiency and fake reduction of the Level-1 Tile-Muon Trigger as a function of TileCal cell energy sum threshold (a) A side (b) C side.	60
Figure 37 – Muon detection efficiency and fake reduction of the Level-1 Tile-Muon Trigger as a function of TileCal cell energy sum threshold for module EBC25.	61
Figure 38 – Muon detection efficiency and fake reduction of the Level-1 Tile-Muon Trigger as a function of TileCal cell energy sum threshold for module EBA43.	62

LIST OF TABLES

Table 1 – Four possible states for a detector.	44
--	----

ACRONYMS

ALICE A Large Ion Collider Experiment

ATLAS A Toroidal LHC Apparatus

AWG Additive White Gaussian

BCs Bunch Crossings

CERN European Organization for Nuclear Research

CIS Charge Injection System

CMS Compact Muon Solenoid

CS Cesium System

CSC Cathode Strip Chambers

DAQ Data Acquisition

DSPs Digital Signal Processors

EM Electromagnetic

FIR Finite Impulse Response

FPGA Field Programmable Gate Array

GeV Giga electron Volt

Glink Gigabit link

HEP High Energy Physics

HLT High-Level Trigger

ICs Integrated Circuits

ID Inner Tracking Detector

IP Interaction Point

L1Calo Level 1 Calorimeter Trigger

L2 Level 2 Selection

LAr Liquid Argon

LHC Large Hadron Collider

LHCb Large Hadron Collider beauty

LVL1 First Level Trigger

MAP Maximum A Posteriori

MDT Monitored Drift Tube

MeV Mega Electron Volt

MF Matched Filter

ML Maximum Likelihood

MLP Multilayer Perceptron

MS Muon Spectrometer

NN Neural Networks

SNR Signal-to-Noise Ratio

OF Optimal Filtering

PDF Probability Density Function

PM Photomultiplier

PMTs Photomultiplier Tubes

ROC Receiver Operating Characteristic

ROD Read-Out Driver

RoI Region of Interest

RPC Resistive Plate Chambers

TeV Tera electron volt

TGC Thin Gap Chambers

TileCal Tile Calorimeter

TTC Trigger Timing and Control

TMDB TileMuon Digitizer Board

CONTENTS

1	Introduction	15
1.1	Motivation and Goals	16
1.2	Main Contributions	17
1.3	Organization of the manuscript	17
2	LHC and the TileMuon Project	19
2.1	CERN	19
2.2	The Large Hadron Collider	19
2.3	The ATLAS Experiment	22
2.4	The ATLAS Calorimetry	24
2.4.1	The Electromagnetic Calorimeter	25
2.4.2	The ATLAS Tile Calorimeter	26
2.5	The Muon Spectrometer	29
2.6	The Trigger System	29
2.7	TileMuon Project	30
2.7.1	TileMuon System Architecture	34
2.7.2	TileMuon Digitizer Board	35
3	Energy Estimation in High Energy Physics Calorimetry	37
3.1	Estimation in Signal Processing	37
3.2	ML Estimator	38
3.3	Energy Measurement in Calorimetry	39
3.3.1	Energy Estimation on TileCal	40
3.3.2	Energy Estimation on LAr	42
3.3.3	Energy Estimation on CMS Electromagnetic Calorimeter	43
4	Energy Estimation for TMDB	44
4.1	Signal Detection	44
4.2	The Matched Filter method	45
4.2.1	Amplitude estimation through the matched filter	46
4.2.2	Matched Filter implementation on FPGA	46
5	TMDB Commissioning Analysis	48
5.1	Database	48
5.2	Noise Characteristics	49
5.3	Pulse Characteristics	51
5.4	Matched Filter Design	52

5.5	Matched Filter Results	54
5.6	System Status	56
6	System Performance	58
6.1	Muon detection efficiency and fake rate reduction	58
7	Conclusions	63
	REFERENCES	65
	APPENDIX A – Scientific Publications	69
A.1	Work published in congress annals	69

1 Introduction

Over the past three decades, electronic instrumentation and signal processing techniques have been widespread in the technological field. They are used in home automation applications, on-board electronics, smart networks in power systems, biomedical instrumentation, not to mention the research advances in chemistry, material science, biology, and clinical medicine.

Modern instruments and instrumentation systems are primarily based on digital techniques. Digital instruments are designed using microcontrollers, microprocessors and dedicated integrated circuits (ICs), which provide them networking, data communications and flexibility in information handling.

Although advanced instrumentation systems became the main cutting edge technology, they also provide many challenges for data processing, such as the amount of data to be processed in a small time.

Advanced instruments and instrumentation methods are widely applied in experimental particle physics. One of the main instruments used in these experiments is the calorimetry system. It is designed to absorb and measure the energy of incident particles. The information provided by the calorimetry systems is used in offline analysis to extract and understand signal and background, and ultimately to improve the understanding of physics models.

In these experiments, the online data processing and trigger/data acquisition (DAQ) have to be optimized for a number of physics channels, large compression factors and to operate with high efficiency, which introduces additional difficulties in its online/offline instrumentation.

A calorimeter consists of a block of matter sufficiently thick to absorb all the energy of incoming particles. Although a portion of the initial energy is dissipated as heat, some fraction of the deposited energy is detectable in the form of signal (e.g. scintillation light, Cherenkov light, or ionization charge), which is proportional to the initial energy. The calorimeter is segmented into a number of cells to acquire information of the energy deposition profiles. Currently used calorimeters can have thousands of cells. Each type of particle has a specific deposition profile in the calorimeter and this is taken into account in the detector design.

The incident particle properties can be measured through the energy deposited by the charged particles' shower in all active cells of the calorimeter. The energy deposited in each cell is measured through its dedicated readout electronics, usually composed by a transducer which converts light into electrical signal, an amplifier, a signal shaping circuit and an analog to digital converter.

Typically, the calorimeter signal pulse is the output of an analog signal shaping circuit. It provides a stable pulse shape whose amplitudes proportional to the energy deposited by the particles. The signal and its energy can be measured through a pulse amplitude estimation technique.

1.1 Motivation and Goals

This work was developed within the ATLAS experiment at the LHC, a general-purpose experiment with a forward-backward symmetric cylindrical geometry and near 4π coverage in solid angle¹. It consists of an inner tracking detector surrounded by a thin superconducting solenoid providing a 2 T axial magnetic field, electromagnetic and hadronic calorimeters, and a muon spectrometer. The inner tracking detector (ID) covers the pseudorapidity range $|\eta| < 2.5$. It consists of silicon pixel, silicon microstrip, and transition-radiation tracking detectors. Lead/liquid-argon (LAr) sampling calorimeters provide electromagnetic (EM) energy measurements with high granularity. A hadronic (steel/scintillator-tile) calorimeter (TileCal) covers the central pseudorapidity range ($|\eta| < 1.7$). The endcap and forward regions are instrumented with LAr calorimeters for EM and hadronic energy measurements up to $|\eta| = 4.9$. The total thickness of the EM calorimeter is more than twenty radiation lengths. The muon spectrometer (MS) surrounds the calorimeters and is based on three large superconducting air-core toroids with eight coils each. The field integral of the toroids ranges between 2.0 and 6.0 $T.m$ for most of the detector. It includes a system of precision tracking chambers and fast detectors for triggering. A dedicated online filter (trigger) system is used to select events and it is implemented in two sequential levels of signal provisions. The first-level trigger is implemented in hardware and uses the calorimeter (coarse granularity) and muon detectors to reduce the accepted event rate from 40 MHz to below 100 kHz. This is followed by a software-based trigger that reduces the accepted event rate to 1 kHz, on average.

During the LHC Run 1 operation (2009 - 2012) were observed a level-1 muon trigger background in the endcap region. The main source of this fake muons are low-momentum protons emerging from the endcap toroid magnets and the beam shielding [1]. The effective bandwidth limitation can be reduced through the coincidence of the TileCal outermost layer signal in the extended barrel region with the end-cap muon chambers. Therefore, a dedicated embedded system, the TileMuon, was developed to assist the muon trigger adding TileCal outermost layer signal information. The system for the extended

¹ ATLAS uses a right-handed coordinate system with its origin at the nominal interaction point (IP) in the centre of the detector and the z -axis along the beam pipe. The x -axis points from the IP to the centre of the LHC ring, and the y -axis points upwards. Cylindrical coordinates (r, θ) are used in the transverse plane, ϕ being the azimuthal angle around the z -axis. The pseudorapidity is defined in terms of the polar angle θ as $\eta = -\ln \tan \theta/2$. Angular distance is measured in units of $\Delta R = \sqrt{\Delta\eta^2 + \Delta\phi^2}$

barrel is foreseen to operate during LHC Run 2 (2015 - 2018) and Run 3 (2019 - 2021) operation.

A TileCal signal processor module receives, processes and send trigger inputs to the Level-1 Muon Trigger, the TileMuon Digitizer Board (TMDB), and is currently installed in ATLAS since July 2015. The activation of the TileCal outermost layer covering $1.0 < |\eta| < 1.3$ to assist the Level-1 Muon Trigger is an important part of ATLAS Phase-0 upgrade program.

This dissertation proposes the muon identification method on the TMDB and evaluates its performance using a dataset from LHC collisions. Additionally, the TMDB operation status in the ATLAS experiment is characterized and the TileMuon system performance is evaluated.

1.2 Main Contributions

1. Studies concerning the signal shape and noise provided for all TMDB channels from LHC collisions dataset.
2. The proposed estimation method, designed for each channel through a pulse shape and noise distribution, provided by a dataset from LHC collisions.
3. The TMDB operation performance evaluation, using a dataset from TileMuon commissioning stage. The TMDB channels were classified concerning their noise amplitude, the online estimation operation was verified, as well as the pulse stability for different data acquisitions.
4. The evaluation of the estimation method applied on TMDB performance.

1.3 Organization of the manuscript

The manuscript is organized as follows. Chapter 2 describes the technical design of the LHC and ATLAS experiments, with particular focus on its calorimeters. The chapter concludes with a concise TileMuon project description to introduce the reader to the scope of this work.

Chapter 3 presents the general concepts of energy reconstruction in calorimetry for high energy physics. The classical parameter estimation method is reviewed as well as the current method to detect and estimate the particle's energy used on TileCal. The energy reconstruction methods used in other calorimeters are also discussed on this chapter.

Chapter 4 focuses on the energy estimation method based on the matched filter theory, the method proposed on this dissertation. The detection of a signal transmitted

through a channel that introduces an additive noise problem is presented as well as the procedure to provide the energy estimate from the signal detectors output.

Chapter 5 summarizes the results of the TileMuon commissioning stage. Studies with TileMuon Digitizer Board datasets are presented to provide the system operation performance as well as the application environment of the estimation method.

Chapter 6 presents the results of the system performance. The muon detection efficiency and fake rate reduction acquired in the commissioning stage are evaluated and compared with the system performance specified during system design.

The final chapter concludes the manuscript with a discussion of the results, perspectives and future work.

2 LHC and the TileMuon Project

The aim of this chapter is to introduce CERN, the LHC accelerator, and the ATLAS experiment. A brief description of the ATLAS subsystems is presented, focusing on the calorimeter system. In addition, the ATLAS trigger system is described, as well as the TileMuon project.

2.1 CERN

Founded in 1954, the European Organization for Nuclear Research (CERN) [2] is the world's biggest physics laboratory with researches devoted to probe the fundamental structure of the universe. CERN sits astride the French-Swiss border near Geneva and currently has 23 member states and about 2500 people working as directly employees, not to mention more than 600 universities and institutes worldwide which contributes with their researches. At CERN, the basic constituents of matter - the fundamental particles - and their interactions are studied using data coming from a particle acelerator complex.

The CERN acelerator complex brings particles (such as protons or ions) close to the speed of light. In 1957, the first particle accelerator was built at CERN to provide beam to the first CERN experiment in particle and nuclear physics. Nowadays, CERN has the most porwerful and the world's lagest particle accelerator, the Large Hadron Collider (LHC) [3].

2.2 The Large Hadron Collider

The LHC has been operating since 2010. A complex of accelerators, shown in Figure 1, work together to push particles to nearly the speed of light. Each machine in the chain increases the energy of particle beams before delivering them to the next, more powerful, accelerator. The collision energy ranges from 0.9 to 13 TeV, with a bunch spacing of 50 and 25 ns.

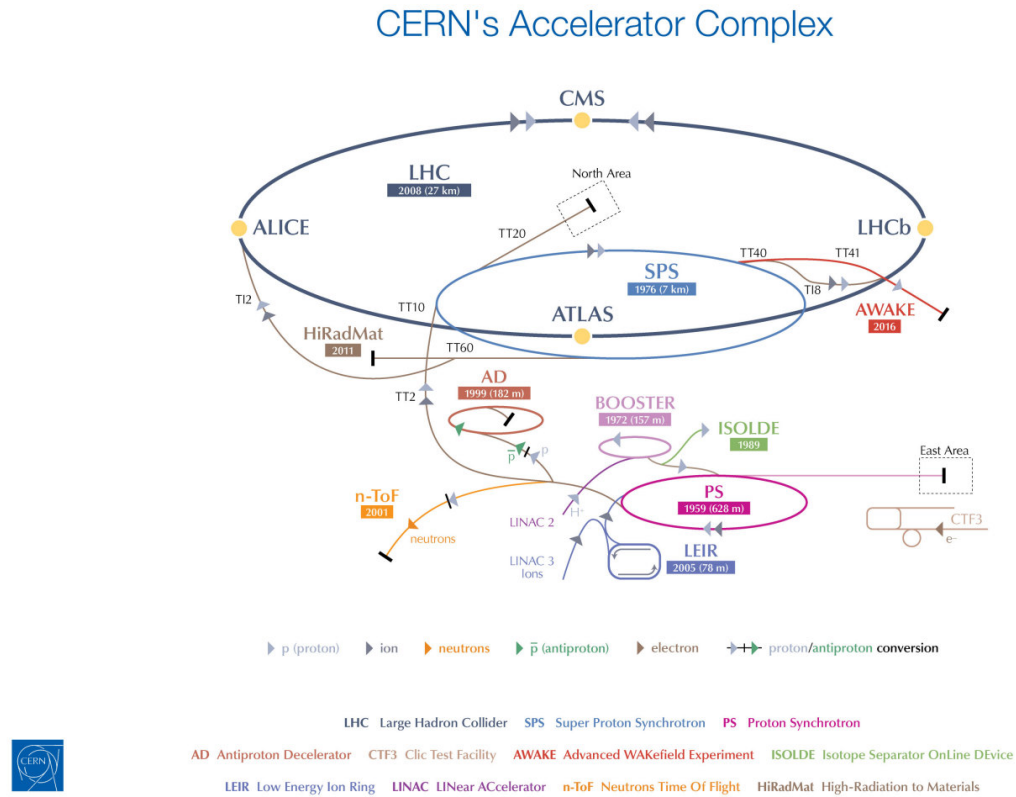


Figure 1: CERN's Accelerator complex (Extracted from [4]).

The LHC is placed in an underground tunnel 27 kilometer in circumference, which is situated between 45m and 170m beneath the soil. The LHC is designed to operate at center-of-mass energy of up to $\sqrt{s} = 14$ TeV for proton-proton collisions.

The collider has four collision points, around which detectors are positioned to observe and record the processes results. Figure 2 illustrates the LHC and four of its main detectors.

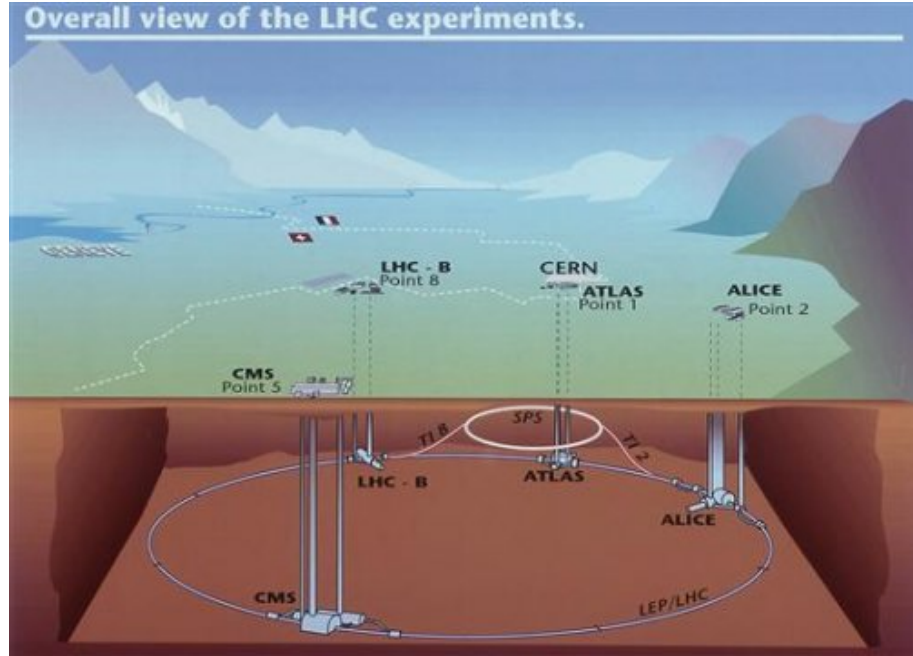


Figure 2: Overall view of the LHC experiments (Extracted from [5]).

The detectors aim is to find information about particles such as their charge, energy and mass, in order to provide clues about the particle's identity. The LHC has four main detectors, each one designed for a specific purpose:

1. **ATLAS** (*A toroidal LHC Apparatus*) [6]

ATLAS is a general-purpose detector optimized to study the greatest possible number of particles that could arise from the LHC collisions.

2. **CMS** (*Compact Muon Solenoid*)[7]

As ATLAS, CMS is a general-purpose detector, built to study the Higgs boson, supersymmetric particles and heavy ion physics.

3. **ALICE** (*A Large Ion Collider Experiment*) [8]

ALICE is the only detector entirely devoted to heavy ions collisions. Its main goal is to unveil the properties of quark-gluon plasma, a state of matter believed to have been formed a few milliseconds after the Big Bang.

4. **LHCb** (*Large Hadron Collider beauty*) [9]

LHCb is devoted to research on the existent asymmetry between the matter and antimatter in the universe.

2.3 The ATLAS Experiment

The ATLAS detector, shown in Figure 3, is a general apparatus designed for precision Standard Model measurements and to search for physics beyond the Standard Model [10]. It comprises six different subsystems: the Inner Detector [11], the Solenoidal Magnets, the Electromagnetic and Hadronic [12] Calorimeters, the Toroid Magnets and the Muon Spectrometer [13].

ATLAS has a forward - backward symmetric cylindrical geometry with dimensions about 45 meters long, 25 meters in diameter and weights 7,000 tonnes, which is similar to the weight of the Eiffel Tower and half as big as the Notre Dame Cathedral in Paris. Its cylindrical geometry covers almost the entire solid angle around the interaction point. Therefore, a cylindrical coordinate system is used to describe the ATLAS experiment, depicted in Figure 4. The azimuthal angle $\phi \in [-\pi, \pi]$ is measured around the axis z and the pseudorapidity $\eta = -\ln \tan(\theta/2)$ invariant under longitudinal boosts in z - direction.

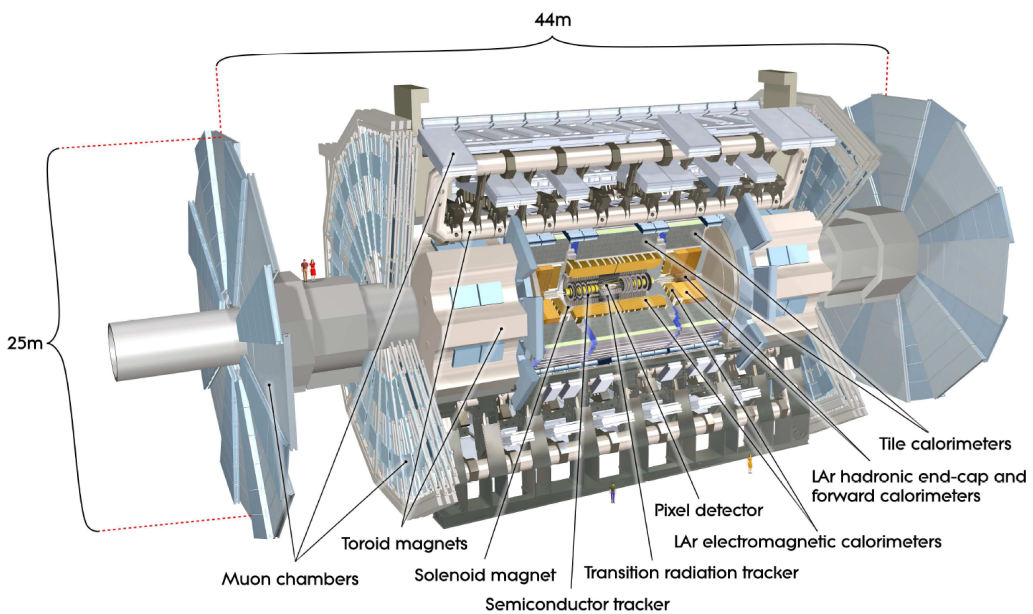


Figure 3: Basic Structure of the ATLAS experiment (Extracted from [14]).

Figure 5 illustrates the particles' signatures in the ATLAS detector. Each particle leaves a specific signature in one or more of the detector sub-systems. The combination of all sub-detector information provides the particle four-momentum.

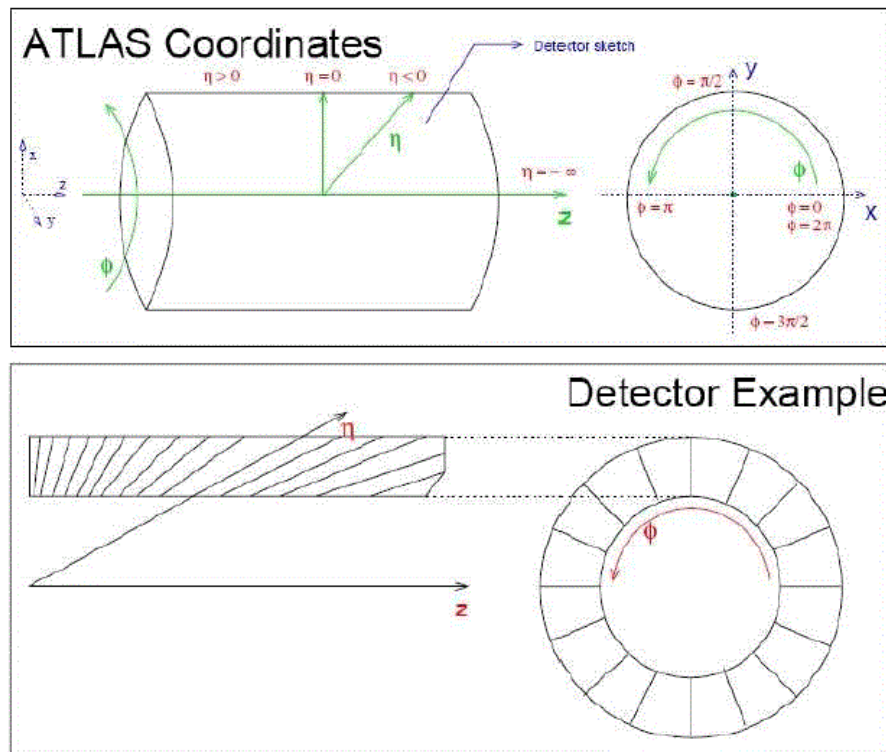


Figure 4: ATLAS coordinate system.

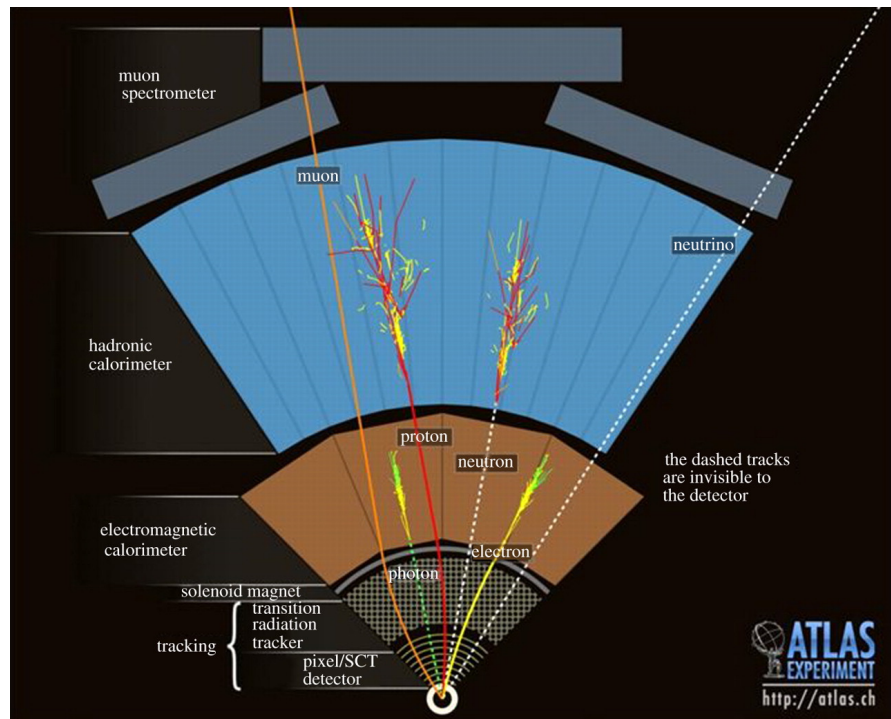


Figure 5: Transverse view of the ATLAS, showing the detection strategy (Extracted from [15]).

ATLAS also uses a specialised multi-level online filtering system, in order to select events interesting for physics analyses - the Trigger System - (described in Section 2.6).

2.4 The ATLAS Calorimetry

In particle physics, calorimetry is an ubiquitous method designed to absorb and measure the energy of particles [16]. Conceptually, a calorimeter is a block of matter which an incident particle interacts and deposits all its energy in a shower of particles with decreases energy [17]. Most of the energy deposited by a charged particles is dissipated and appears in form of heat in the active part of the calorimeter. The energy can then be detected in the form of a sampling/homogeneous signal (e.g. charge or light), which is proportional to the initial energy.

Calorimeters can be broadly classified concerning their technical structure into sampling calorimeters and homogeneous calorimeters. Sampling calorimeters are devices in which the energy degradation of the incident particle and the energy measurement are separated in intercalating layers of different materials. On the other hand, homogeneous calorimeters are composed of only one type of material, which causes the energy degradation and signal generation. Calorimeters are interesting in particle physics for several reasons:

1. The calorimeter energy resolution improves with the energy of the incident particle.
2. Calorimeters can be sensitive to neutral and charged particles. Weakly interacting particles, such as neutrinos, can then be inferred through the missing energy in the event.
3. Calorimeters are versatile detectors. Although designed to measure energy, they can be used to identify different particles, to measure the particle's arrival time and detect the shower direction and position.
4. Their fast time response allows application in high-speed signals and a smooth online event selection process.
5. The length of the detector increases logarithmically with particle energy.

The ATLAS calorimetry system has been developed to absorb most of hadrons, leptons and photons interacting with matter. Motivated by this purpose, high granularity liquid-argon (LAr) electromagnetic (EM) and hadronic sampling calorimeters are installed, as shown in Figure 6.

The hadronic calorimeter provides the energy measure of hadrons that lose their energy through particle showers, whereas the electromagnetic calorimeter provides

electromagnetic energy measurements of electrons and photons. Calorimeters can absorb most known particles, except muons and neutrinos [18].

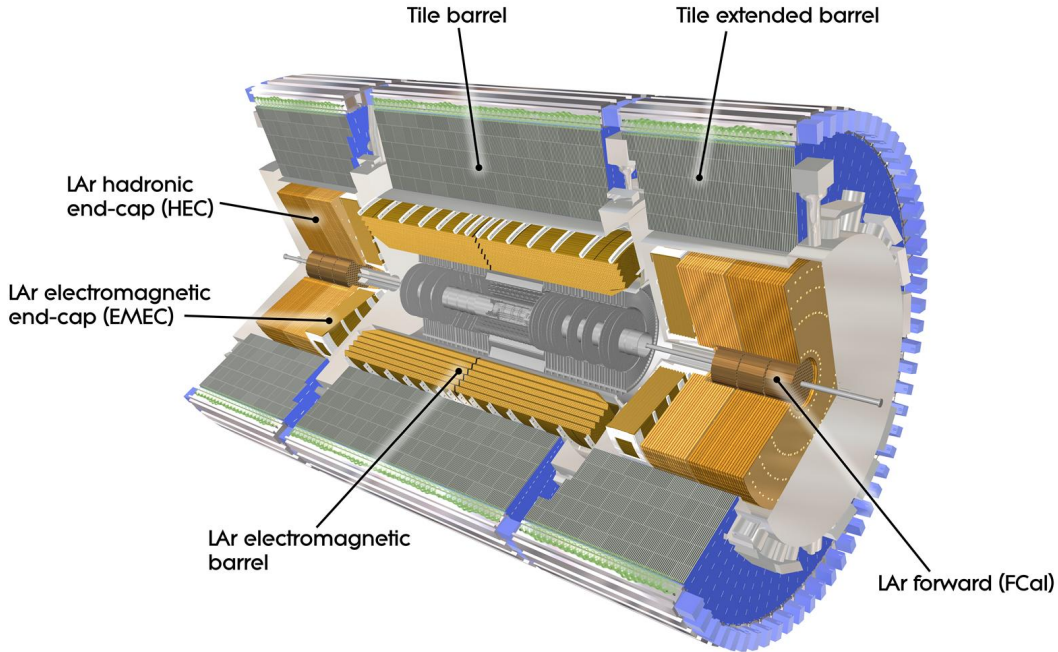


Figure 6: A computer generated image of the full calorimeter (Extracted from [15]).

2.4.1 The Electromagnetic Calorimeter

The Liquid Argon calorimeter (LAr) [19] is the electromagnetic (EM) calorimeter of ATLAS. It has an accordion geometry, i.e. lead absorber plates over its full coverage and accordion-shaped kapton electrodes immersed in liquid Argon. The design provides full ϕ symmetry without azimuthal cracks.

LAr comprises a barrel and two end-cap components. The calorimeter shape consists of two identical half-barrels, separated by a 6 mm gap at $z = 0$ and centered around the collision point $|\eta| < 1.475$. Each end-cap is physically splitted into two coaxial wheels covering the region $1.375 < |\eta| < 3.2$.

Each barrel module of the EM calorimeter, depicted in Figure 7, is segmented in three samplings in depth. The first sampling has a fine granularity, which provides precise measurements of the incident energy of EM showers started by photons and electrons. The middle sampling is responsible to absorb most of energy of the EM shower. The third sampling, less segmented in η , identify EM and hadronic showers.

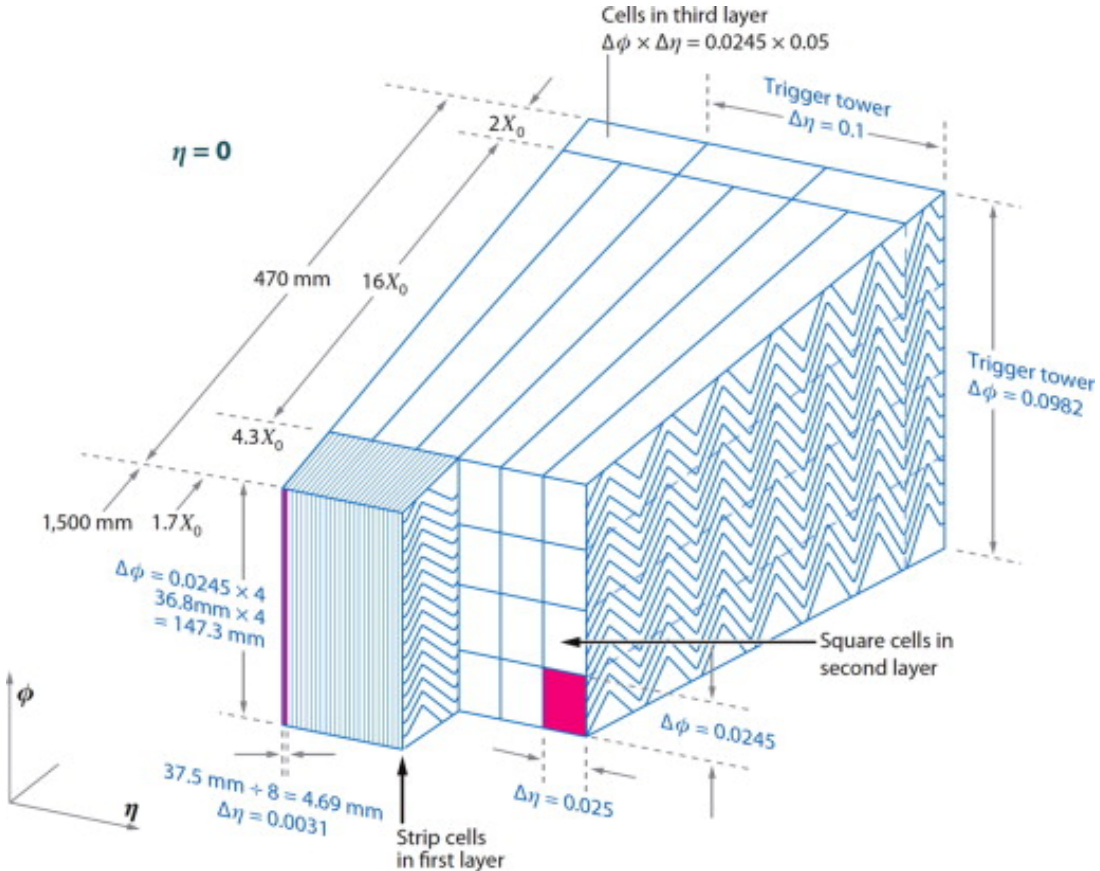


Figure 7: Segmentation of the EM calorimeter of ATLAS.((Extracted from [19])

2.4.2 The ATLAS Tile Calorimeter

The Tile Calorimeter (TileCal) [20] is located directly outside of the LAr and consists of the central hadronic section of the ATLAS calorimeter. It is a sampling device that uses steel as absorber material and scintillating tiles as active material [20] to provide precise measurements of hadrons, taus, jets and missing transverse energy.

Figure 8 illustrates the system structure of one of the 256 ϕ wedges of TileCal. The hadron particle produced in the collision point travels through the calorimeter and produces light proportional to the energy deposited by the particle in the scintillating tiles. The light is transmitted by wavelength shifting fibers and read out by photomultiplier tubes (PMTs), which generate the electrical signal to be processed.

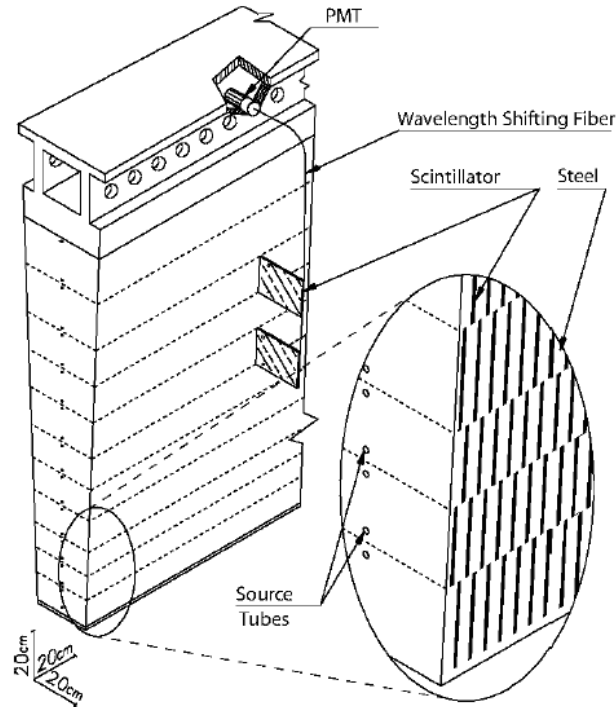


Figure 8: The Tile calorimeter design principle (Extracted from [14]).

TileCal comprises a central barrel and two extended barrels azimuthally divided into 64 modules of granularity $\Delta\phi = 0.1$. Each module from both central and extended barrels is respectively divided into 23 and 16 cells, which consists of approximately 5000 cells, each one readout by two channels.

Similar to the LAr, the TileCal is segmented in depth in three layers, illustrated in Figure 9. The TileCal trigger towers are built by adding signals from the three sampling layers and the resulting added signals are sent to the first trigger level (LVL1) of ATLAS.

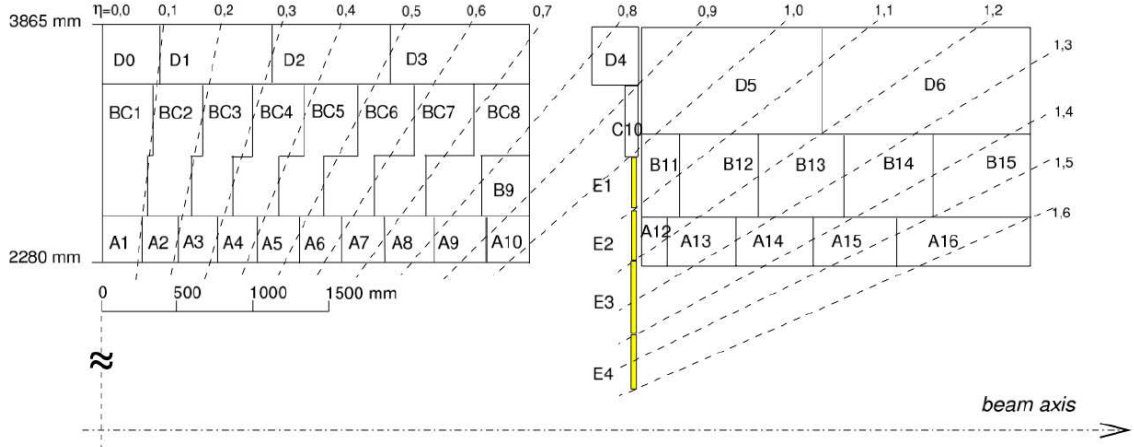


Figure 9: The calorimeter segmentation for one module of the barrel ($\eta > 0$) and one module of the extended barrel (Extracted from [21]).

The current TileCal readout signal chain is illustrated in Figure 10. The light produced in the scintillating tiles is sent by optical fibers to the light mixers and distributed over the fibers leading to the photomultiplier tube (PMT) where it is converted to an electrical signal. The 3-in-1 card (Front-End Board) is responsible for the signal conditioning and amplification providing three analog signals as output. Two signals outputs (high and low gain) are digitized in the Digitizer Boards and sent via high speed optical links (Interface Board) to the TileCal back-end electronics. The Read-Out Driver (ROD) is the main back-end electronics component, as it performs preprocessing and send the signal to the second level trigger [22].

The TileCal calibration system comprises:

1. Charge Injection System (CIS) [23]: The CIS generates pulses from discharged capacitors in the read-out circuit to simulate physics signals in TileCal and measures the electronic response. Therefore, a quantitative relationship between the electronic response of TileCal readout channels and the analog signals from the Tile Calorimeter can be provided.
2. Laser System [24]: The laser calibration system sends a controlled optical amount of light from a laser to monitor each TileCal PMT and the photodiodes simultaneously. It provides the PMT with the gain measurement used for timing calibration, monitoring of TileCal and PMTs gain adjustments.
3. Cesium system (Cs) [25]: The Cesium system introduces a $\gamma^{137}C$ through all the tiles to equalize the individual channel response and monitor stability of optics elements.

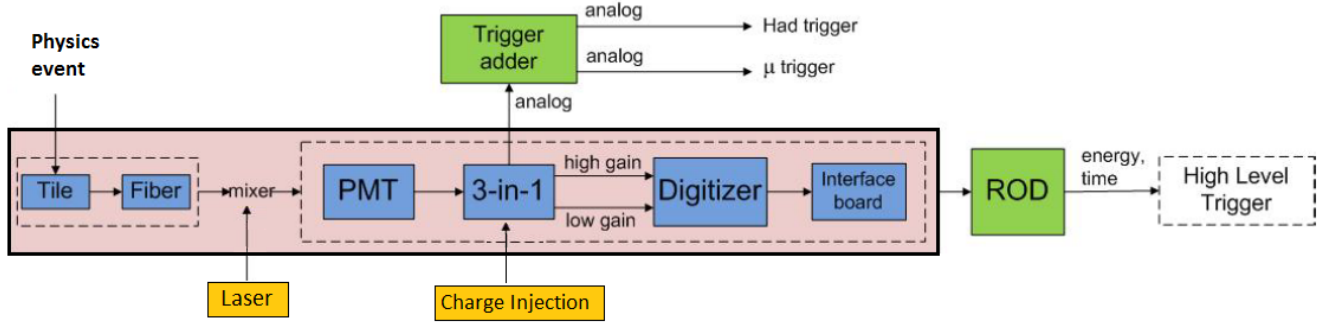


Figure 10: TileCal Readout Signal Chain (Extracted from [22]).

2.5 The Muon Spectrometer

The Muon Spectrometer (MS) [18] is the outermost detector of ATLAS. It is designed to detect muons, a particle which cannot be stopped by the previous components of ATLAS, with a high precision.

The MS comprises a long barrel and two inserted end-cap magnets equipped with two types of fast triggering chambers, the Resistive Plate Chambers (RPC) and the Thin Gap Chambers (TGC). It also uses three layers of hight precision tracking chambers, i.e. Monitored Drift Tube (MDT) and Cathode Strip Chambers (CSC) to provide precise tracking and momentum measurement of muon candidates.

2.6 The Trigger System

The high LHC collision rate, of approximately 40 MHz at 25ns bunch spacing, makes impractical to record every event. An online event selection is employed to reduce the rate of events recorded while maintaining the highest efficiency for all analysis of interest.

Figure 11 gives an overview of the Trigger system of ATLAS. Is is structured in a 2-level architecture, Level-1 and the Level-2 and the high-level trigger (HLT). Each trigger level employs an additional selection criteria refining the decisions made at the previous one. Finally, a thousand events per second is recorded to permanent storage.

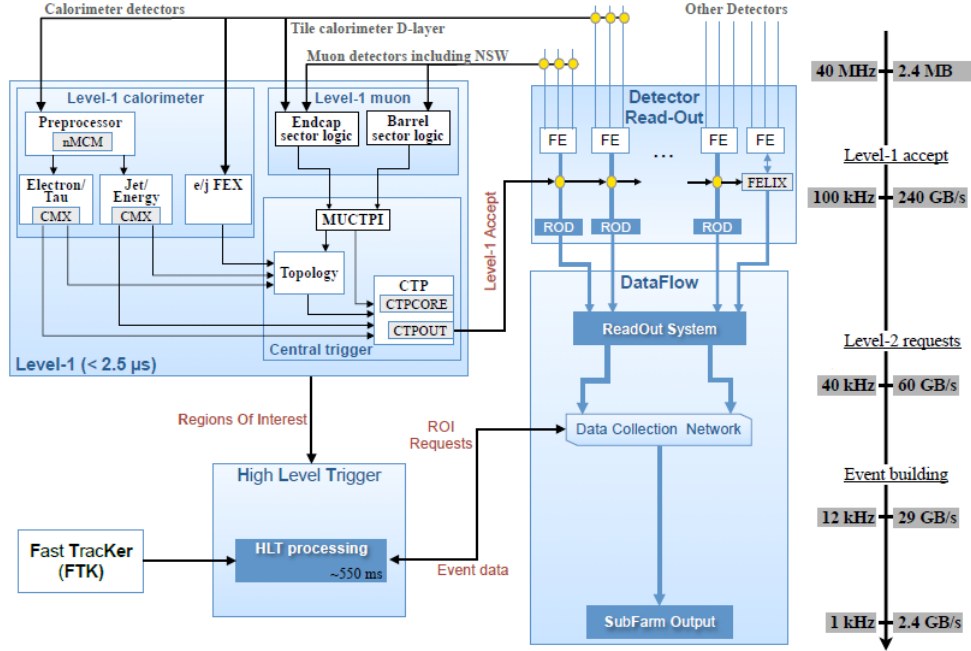


Figure 11: Schematic overview of the Trigger and DAQ system (Extracted from [26]).

The Level-1 calorimeter trigger (L1Calo) is hardware-implemented and processes signals from the hadronic and electromagnetic calorimeters in real-time to reduce the incoming bunch crossing rate to 100 kHz. The high-level trigger is software implemented, and operates on a large farm of commercial computer processors. It executes chains of reconstruction and signature algorithms that analyze the properties of the events.

2.7 TileMuon Project

The TileMuon project aims at using the TileCal outermost layer (D cells) signal in the extended barrel region to reduce the fake muon trigger rate due to slow charged particles [27], i.e. protons emerging from the end-cap toroid and beam shielding interactions with the muon detector.

Figure 12 illustrates a transversal cut in the ATLAS detector. The emergent muons from collisions cross the TileCal extended barrel region, covered by $1.0 < |\eta| < 1.3$, before reaching the TGC.

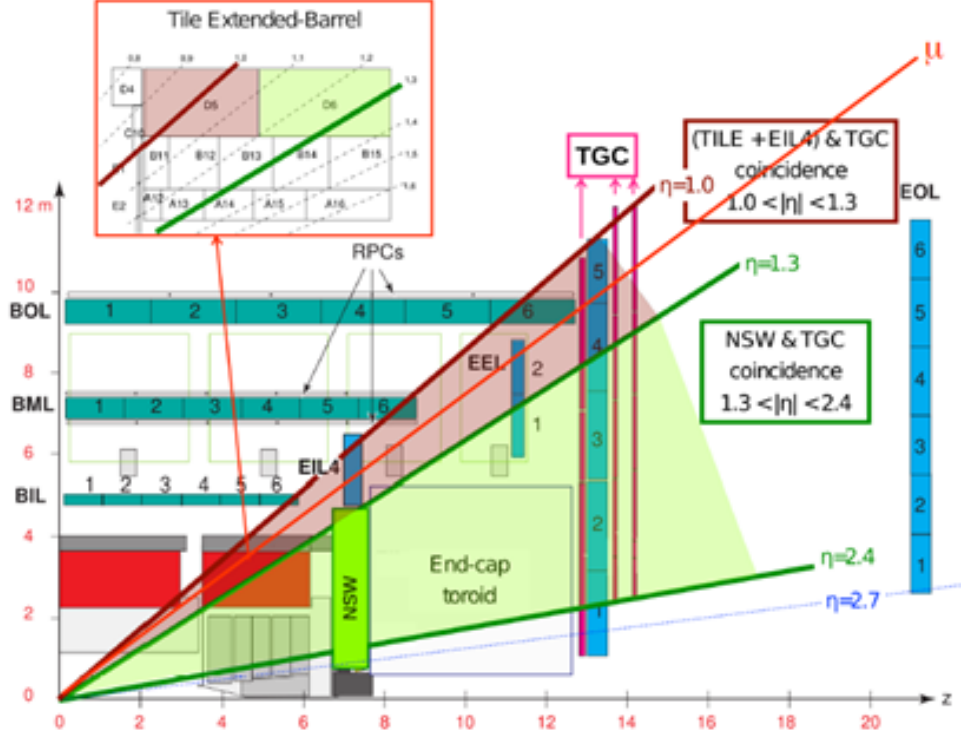


Figure 12: Illustration of the coincidence between TileCal extended barrel and the end-cap muon chamber (Extracted from [21]).

The distribution of Level-1 muons as a function of η above an online momentum (p_T) threshold of 20 GeV is shown in Figure 13. The combined information between the TileCal extended barrel and TGC improves the trigger muon efficiency. The TileCal signal is received, processed and sent to the muon trigger logic by a new electronic system currently installed in ATLAS.

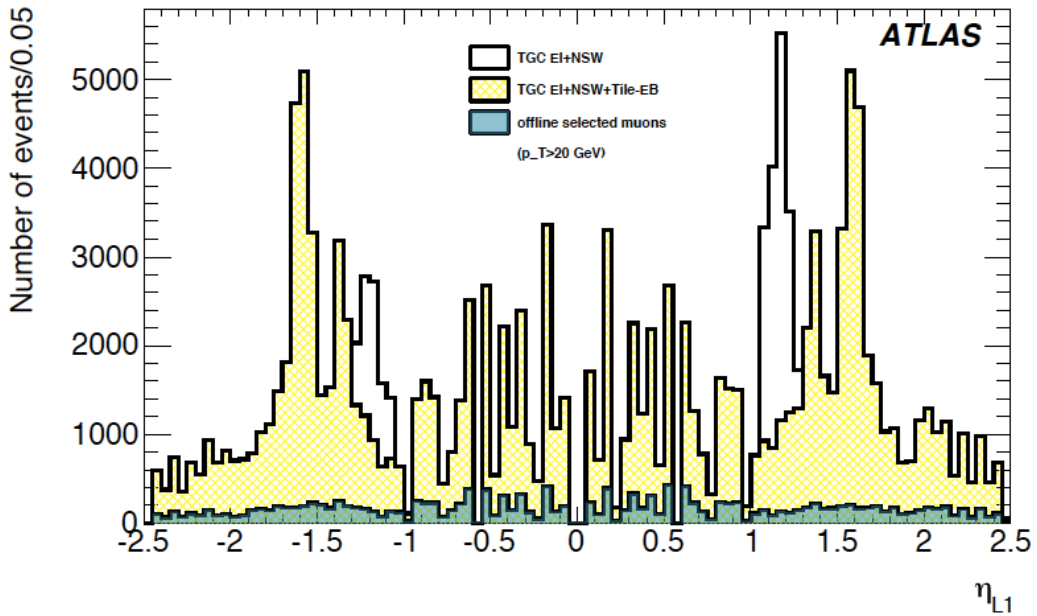


Figure 13: Distribution of Level-1 muons as a function of η and for a p_T threshold of 20 GeV. The combined yellow (shaded) and white (un-shaded) distribution is with the NSW included in the Level-1 muon endcap decision. The yellow (shaded) distribution alone shows the effect of including the outer layer of the TileCal extended barrel in the Level-1 muon endcap decision. (The underlying cyan (dark-shaded) distribution represents offline reconstructed muons after an offline 25 GeV p_T cut). Extracted from [28]).

The reconstruction efficiency for combined muons with an offline p_T greater than 25 GeV (open red circles) is compared with events triggered by Level-1 muons (open blue squares), depicted in Figure 14, as a function of the TileCal cell energy threshold. The muon detection efficiency is kept around 97% with a rate reduction around 80% when a 500 MeV energy cut is applied. Therefore, the muon detection efficiency and rate reduction are acceptable even with a higher TileCal muon signal to noise rate.

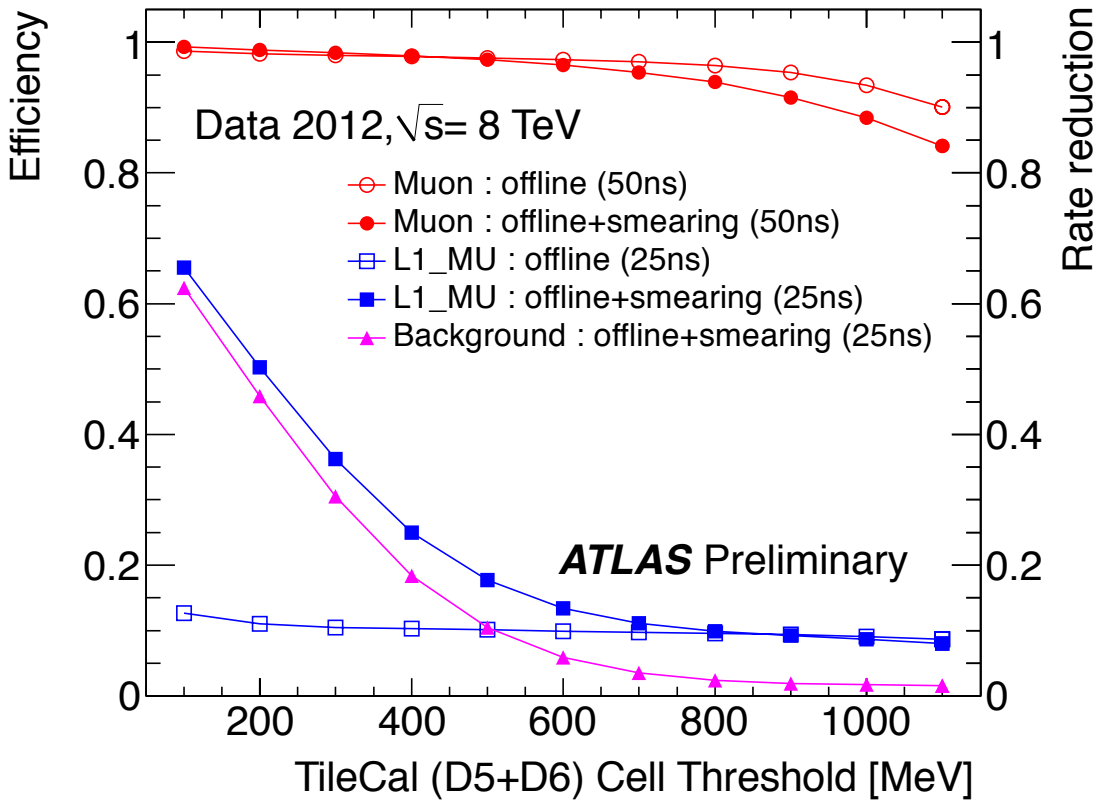


Figure 14: Muon detection efficiency and Level-1 muons rate reduction as a function of TileCal cell energy sum threshold. False alarm values are also shown, giving the probability that in each bunch crossing the sum of the energies deposited in D5 and D6 will be over threshold. Results were obtained using standard offline readout data. A smearing of 200 MeV was introduced in the response of each cell to simulate the electronics noise of the Level-1 readout. Extracted from [28].

Figure 15 shows the muon detection efficiency (black dots) and muon fake reduction (red triangles) as a function of the energy threshold applied to the D5+D6 TileCal cells energy, obtained with a prototype receiver module used in 2010-2011 data taking, and connected to the level 1 calorimeter trigger electronics. Using a threshold cut of 500 MeV, muon detection efficiency of 93% and 17% of fake muons are achieved. The measured efficiency is lower than that presented in Figure 14 and this is probably due to the selection being made on the sum of the raw D5 and D6 analogue signals rather than on the sum of individually calibrated cell.

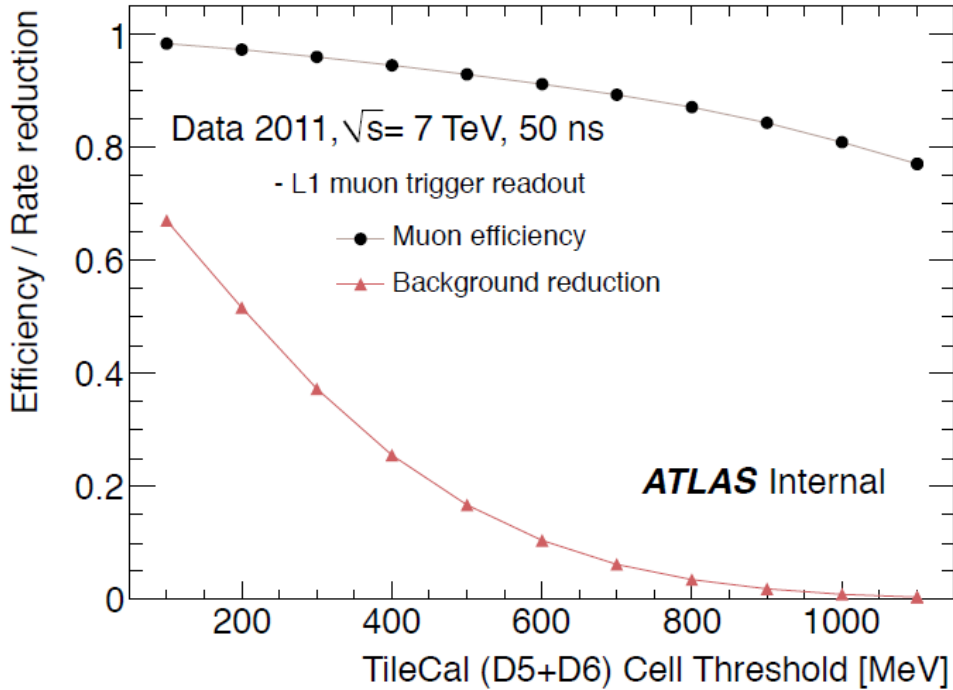


Figure 15: Muon detection efficiency and rate reduction as a function of TileCal cell energy sum threshold. Extracted from [22].

2.7.1 TileMuon System Architecture

The TileMuon System consists of 64 modules from the TileCal extended barrel and the Level 1 muon trigger in the endcap region, divided into 48 trigger sectors. A hight- p_T muon should cross one of the two TileCal modules in front of the endcap trigger sector in which a signal has been produced.

The TileMuon Digitizer Board (TMDB) module was developed to process the D5 and D6 signals from 8 TileCal modules and interface with 3 Level-1 muon endcap sector logic blocks. Therefore, the TileMuon system, illustrated in Figure 16, is composed of 16 TMDB modules hosted in one VME 9U crate in ATLAS USA15 cavern, each one receiving 32 analog muon signals from the TileCal and interfacing with 3 TGC sector logic blocks. The TGC sector logic receives the TMDB information through three Gigabit links (Glink) from TGC inner chambers.

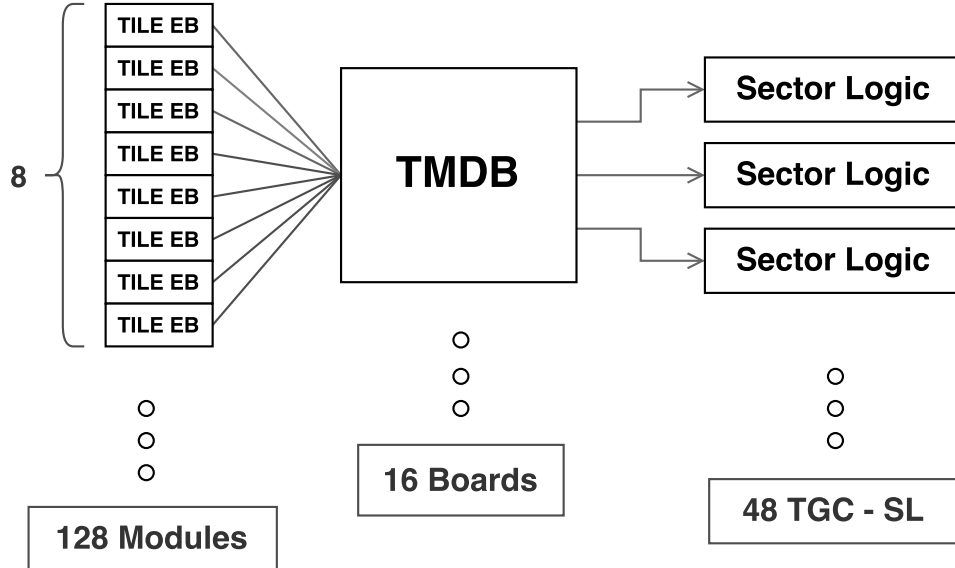


Figure 16: TileMuon System basic architecture.

2.7.2 TileMuon Digitizer Board

Figure 17 illustrates the TMDB design approach. The 32 analogic signals reception and digitization are performed by the signal reception block. The system also comprises a core Field Programmable Gate Array (FPGA), responsible for processing, communication and monitoring, which simplifies the hardware design.

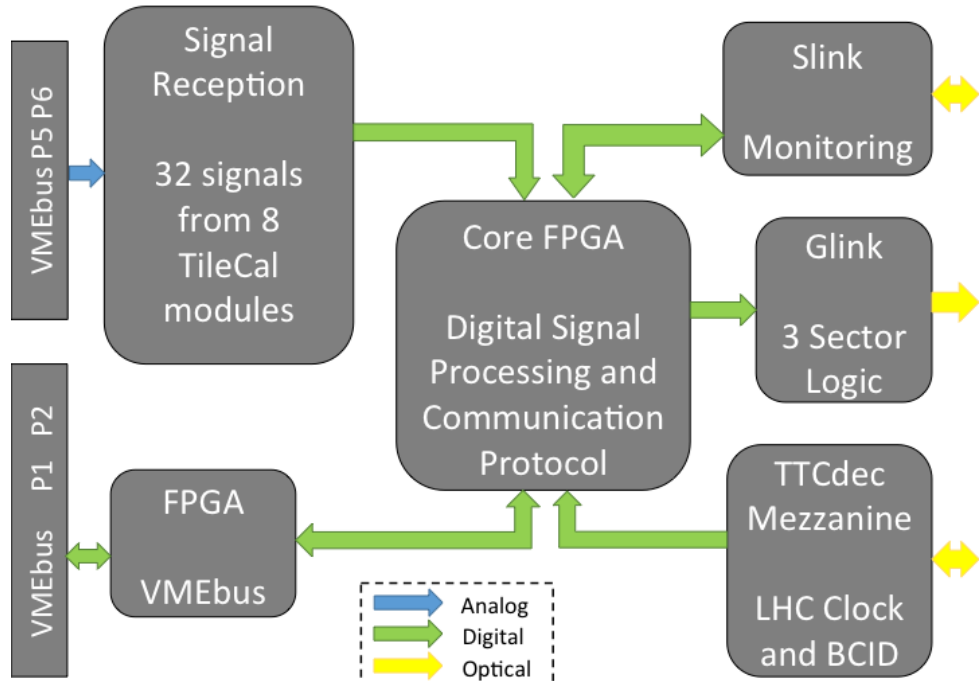


Figure 17: TMDB Design.

A dedicated FPGA is used to provide the communication with the VMEbus and control, monitoring and firmware updates of both FPGAs. The calibration and monitoring functionalities can also be done through the Link interface. The Glink block is responsible for the communication with the 3 TGC sector logic blocks. The TTCdec is a dedicated mezzanine board designed for the ATLAS trigger timing and control (TTC) signal reception and decoding, providing the synchronization with the experiment.

The TMDB output provides the energy value estimated by performing an inner product between the Matched Filter (MF) coefficients and the incoming time samples in ADC counts. Four TMDB decision triggers are obtained from the comparison the energy output and a threshold, two from the D6 cell and two from D5+D6 cells. A peak detector algorithm is used for triggering events in which the readout pulse is within the readout window. The Matched Filter coefficients and thresholds are loaded on TMDB and the trigger muon decision is obtained from the coincidence between Peak-detector and Threshold algorithms.

3 Energy Estimation in High Energy Physics Calorimetry

Over the past decades the energy reconstruction in calorimetry has been formulated as a parameter estimation problem. Therefore, this chapter provides an overview of parameter estimation theory from literature and the energy estimation strategy used on modern calorimetry.

3.1 Estimation in Signal Processing

Most physical processes observed in nature can be represented mathematically. There are several types of mathematical models used for that purpose, such as the deterministic and the stochastic models. A deterministic model has every set of variables uniquely determined by parameters in the model and sets of previous values of these variables. In a stochastic model, randomness is present, and variables are not described by unique values, but rather by probability distributions.

Estimation theory is commonly used to extract information from electronic systems. These systems include: radar, sonar, speech and image analysis, biomedicine, communications, and control. All systems mentioned need to estimate a parameter or a group of parameters of a random process often corrupted by additive noise. Although there are examples that a human interpreter can easily discern, in most cases a human interpreter would be unable to determine the target position from the received waveforms, making estimation systems an indispensable tool [29].

The signal estimation problem can be modeled as the extraction of parameters based on time continuous waveforms. However, the digital signal processing has been extremely widespread over the last years, making the signal estimation a discrete time problem. Consider a N -point dataset $x = x[0], x[1], \dots, x[N - 1]$, which depends on an unknown parameter θ . The goal is to determine θ based on the data, or to define an estimator

$$\hat{\theta} = g(x[0], x[1], \dots, x[N - 1]), \quad (3.1)$$

where g is a function. The first step to design a good estimator is to mathematically model the data. Inherently random data can be described by a probability density function (PDF). The PDF is parameterized on θ . Therefore, a different class of PDF is obtained for a different value of θ .

The estimation based on PDFs is termed classical estimation and its performance depends on the PDF assumptions. This approach assumes the parameters of interest are deterministic but unknown [29].

In cases where some features about the parameter are known a priori, this knowledge can be incorporated to the problem's solution. We can assume, for example, that θ is a random variable and assign it a PDF with an uniform range. Any estimator will yield values in this range and the desired parameter is then viewed as a realization of the random variable θ [29][30].

Estimators based on PDFs usually have no analytical solution, which makes their implementation difficult, requiring a multidimensional optimization or integration. In these situations, is interesting to use alternative estimators, which provide a suboptimal result, but can be implemented on a digital computer. Linear estimators are easy to implement and require low computational complexity. For that reason, linear estimators have been widely used to energy estimation in calorimetry [31][32][33].

3.2 ML Estimator

The Maximum Likelihood estimation is a method designed to estimate the parameters of a statistical model (e.g. the signal amplitude immersed in an additive background noise), which maximizes the probability $P(\theta|x)$, i.e., it finds the $\hat{\theta}$ value providing the highest conditional probability $P(\theta|x)$. Although that probability is usually unknown, according to Bayes' theorem the probability of an event can be described based on prior knowledge of conditions that might be related to the event:

$$P(\theta|x) = p_{X|\Theta}(x|\theta)P(\theta), \quad (3.2)$$

where $p_{X|\Theta}(x|\theta)$ is the conditional probability density function of the event and $P(\theta)$ is a prior probability distribution of θ .

The probability $P(\theta|x)$ is given by the conditional PDF $p_{X|\Theta}(x|\theta)$ maximization, the so-called likelihood function. Suppose the probability density function $p_{\mathbf{r}|\hat{A}_{mle}}(\mathbf{r}|\hat{A}_{mle})$ of a signal sample with N independent and identically distributed observations represented by \mathbf{r} is known, the signal amplitude \hat{A}_{mle} can be estimated using the equation (3.3):

$$\frac{\partial p_{\mathbf{r}|\hat{A}_{mle}}(\mathbf{r}|\hat{A}_{mle})}{\partial \hat{A}_{mle}} = 0. \quad (3.3)$$

In calorimetry, the digitized pulse samples s_k can be often expressed as:

$$r_k = Ag_k + n_k \quad k = 0, 1, 2, \dots, N - 1, \quad (3.4)$$

where A is the true amplitude, g_k is the reference pulse shape sample and n_k is the electronic noise. If the noise can be modeled as a zero-mean Gaussian process with

covariance matrix \mathbf{C} , the probability density function can be written as:

$$p_{\mathbf{r}|\hat{A}_{mle}}(\mathbf{r}|\hat{A}_{mle}) = \frac{1}{\sqrt{2\pi \det(\mathbf{C})}} \exp\left(-\frac{(\mathbf{r} - A\mathbf{g})^T \mathbf{C}^{-1} (\mathbf{r} - A\mathbf{g})}{2}\right). \quad (3.5)$$

Where \mathbf{r} is the received signal vector and \mathbf{g} is the signal of interest vector.

The problem can be solved applying the logarithm and computing the derivatives in Equation (3.5):

$$\frac{\partial p_{\mathbf{r}|\hat{A}_{mle}}(\mathbf{r}|\hat{A}_{mle})}{\partial A} = \frac{-1}{\sqrt{2\pi \det(\mathbf{C})}} \frac{(\mathbf{r} - A\mathbf{g})^T \mathbf{C}^{-1} (\mathbf{r} - A\mathbf{g})}{2} \quad (3.6)$$

The probability density function will be maximized when Equation (3.6) is equal to zero:

$$\hat{A}_{mle} = \frac{\mathbf{r}^T \mathbf{C}^{-1} \mathbf{g}}{\mathbf{g}^T \mathbf{C}^{-1} \mathbf{g}} = \mathbf{r}^T \mathbf{w}_{mle}. \quad (3.7)$$

As a result, the \hat{A}_{mle} estimation can be implemented by a finite impulse response (FIR) filter with \mathbf{w}_{mle} coefficients [34].

In the case where the noise cannot be modeled as Gaussian, the signal joint probability density function should be considered on the estimator project, which provides no analytical solutions and requires high computational effort.

3.3 Energy Measurement in Calorimetry

The most common energy measurement strategy in calorimetry is to estimate the pulse amplitude from signal corrupted by electronic noise through optimization procedures. Calorimeters have thousands of readout channels with a large electronic chain, which produces a typically Gaussian distribution noise. This noise modeling simplifies the amplitude estimator design, once the resulting noise covariance matrix can be used to describes the random process.

The pulse samples are acquired from a readout signal spread along several adjacent Bunch-Crossings (BCs) [35][36][37][38] whose shape is considered to be fixed for the entire dynamic range. Figure 18 illustrates a typical unipolar pulse shape of a calorimeter. The digital samples used in digital processing are highlighted. The goal of energy reconstruction techniques is to estimate the desired signal amplitude (in black) from the digital samples.

The energy reconstruction is typically obtained by a weighted sum of digitized pulse samples. This approach provides an estimation algorithm with a fast response, which is convenient for systems with high event rate. The estimated amplitude is compared to

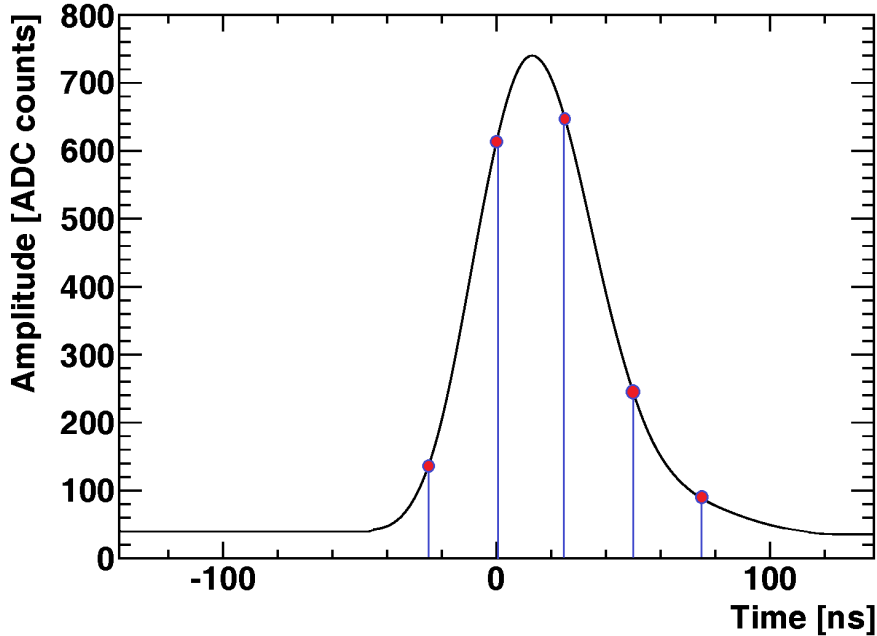


Figure 18: A typical unipolar pulse shape of a calorimeter whose digital samples are extracted from signal.

a threshold and only signals with amplitude values above the threshold are used in the event reconstruction offline analysis.

The following sections describe the energy estimation methods used in ATLAS and CMS calorimeters.

3.3.1 Energy Estimation on TileCal

The Optimal Filtering (OF) [39] algorithm is the method used in both hadronic and electromagnetic calorimeters in ATLAS for energy reconstruction. This technique uses the autocorrelation function of the samples to maximize the signal-to-noise ratio and determine the time origin and the amplitude of the signal. Because the electronic noise may be modeled as a Gaussian process in ATLAS calorimeters, the OF method has been broadly used [40].

The OF algorithm version presented in this work, so called Optimal Filtering 2 [41], has been used on TileCal until 2014 for amplitude estimation. The method was also implemented in liquid ionization calorimeters [31].

In TileCal, \mathbf{g} can be defined as a set of values of the normalized reference pulse shape signal at a time t , $g(t)$. The digitized ADC samples y_i can thus be expressed as [41]:

$$y_i = ped + Ag(t_i + \tau) + n_i, \quad (3.8)$$

where A is the true amplitude, τ represents a phase shift, n_i is the background noise and ped is the signal pedestal.

The algorithm used in Level-1 trigger needs to be simple and fast to meet its timing constraints [42]. Therefore, the approach in ATLAS calorimeter is to minimize the variance of the signal amplitude estimation based on a weighted sum of digitized samples. The estimate of the amplitude can be calculated by:

$$\hat{A} = \sum_{i=1}^N y_i w_i, \quad (3.9)$$

where N is the number of samples and w_i is the OF weights vector computed offline.

The variance to be minimized can be calculated as[43]:

$$var(\hat{A}) = \mathbf{w}^T \mathbf{C} \mathbf{w}, \quad (3.10)$$

where \mathbf{C} is the background covariance matrix and $\mathbf{w} = w_1, \dots, w_N$.

The minimization must be performed under some constraints:

$$\sum_{i=1}^N g_i w_i = 1 \quad (3.11)$$

$$\sum_{i=1}^N g'_i w_i = 0 \quad (3.12)$$

$$\sum_{i=1}^N w_i = 0 \quad (3.13)$$

where g_i is the TileCal reference pulse shape vector and g'_i is its derivative. The first constraint was added to provide unbiased estimations, while both second and third constraints assure the algorithm immunity against phase and baseline fluctuations [43].

With these conditions and using the Lagrange multipliers method the weights w_i can be calculated by solving the following system:

$$\begin{pmatrix} C_{1,1} & \dots & C_{1,7} & g_1 & g'_1 & 1 \\ \vdots & \ddots & \vdots & \vdots & \vdots & \vdots \\ C_{7,1} & \dots & C_{7,7} & -g_7 & -g'_7 & 1 \\ g_1 & \dots & g_7 & 0 & 0 & 0 \\ g'_1 & \dots & g'_7 & 0 & 0 & 0 \\ 1 & \dots & 1 & 0 & 0 & 0 \end{pmatrix} \begin{pmatrix} w_1 \\ \vdots \\ w_7 \\ \lambda \\ \xi \\ v \end{pmatrix} = \begin{pmatrix} 0 \\ \vdots \\ 0 \\ 1 \\ 0 \\ 0 \end{pmatrix}, \quad (3.14)$$

where λ, ξ, v are the Lagrange multipliers.

The covariance matrix \mathbf{C} can be written as an identity matrix if the noise is white. The weights are calculated offline and implemented on Digital Signal Processors (DSPs), which provide the online amplitude estimation for the selected events.

3.3.2 Energy Estimation on LAr

The Liquid Argon calorimeter also uses the OF method to determine the amplitude energy estimation. However, in this case, the third constraint (Equation (3.7)) is removed from the optimization procedure. This method is called OF1. The OF1 algorithm used on LAr computes the baseline value through special runs stored in a database and it subtracts it from each ADC sample. The amplitude estimation is given by:

$$\hat{A} = \sum_{i=1}^N (y_i - ped) w_i. \quad (3.15)$$

Figure 19 illustrates the LAr ionization Pulse Shape. Although 32 samples are used to provide the pulse representation, only 5 samples, located around the pulse peak, are used to estimate the energy.

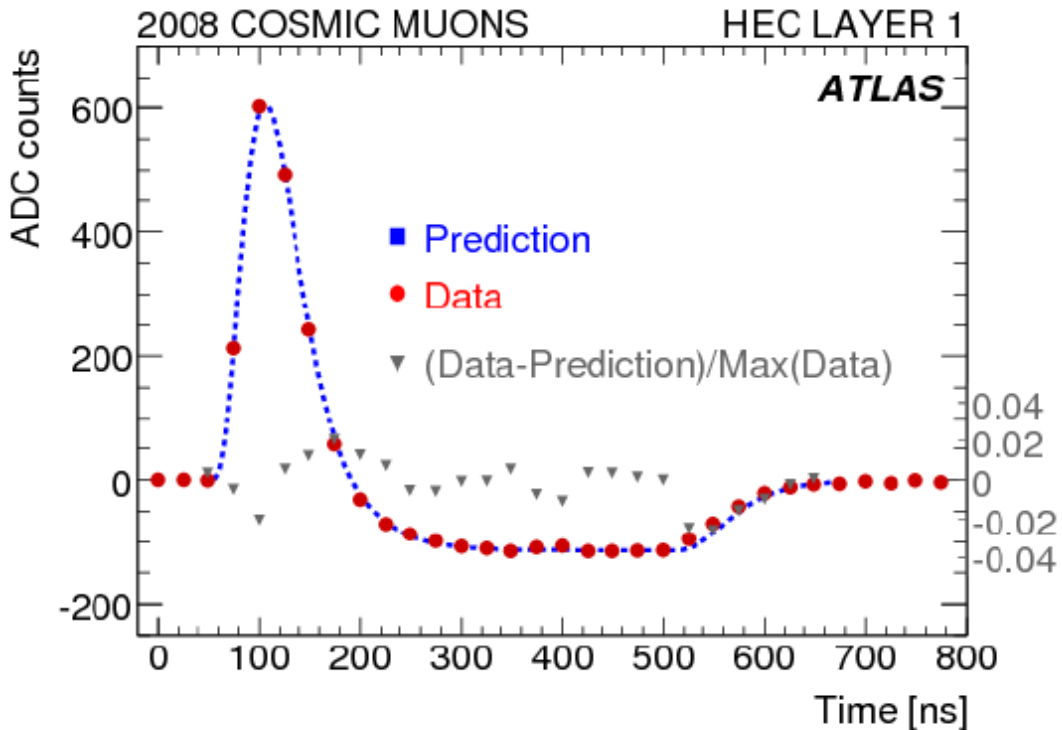


Figure 19: The LAr ionization Pulse Shape (Extracted from [44]).

3.3.3 Energy Estimation on CMS Electromagnetic Calorimeter

As LAr, the CMS electromagnetic calorimeter also uses the OF1 algorithm as the energy estimation method. The difference is that the OF1 implemented on CMS EM calorimeter computes the baseline value event-by-event, while LAr's algorithm computes it through special runs stored in the database. Figure 20 shows the CMS reference pulse and its samples used on digital processing. Notice that the algorithm uses the samples located before the interest peak to estimate the baseline of the signal.

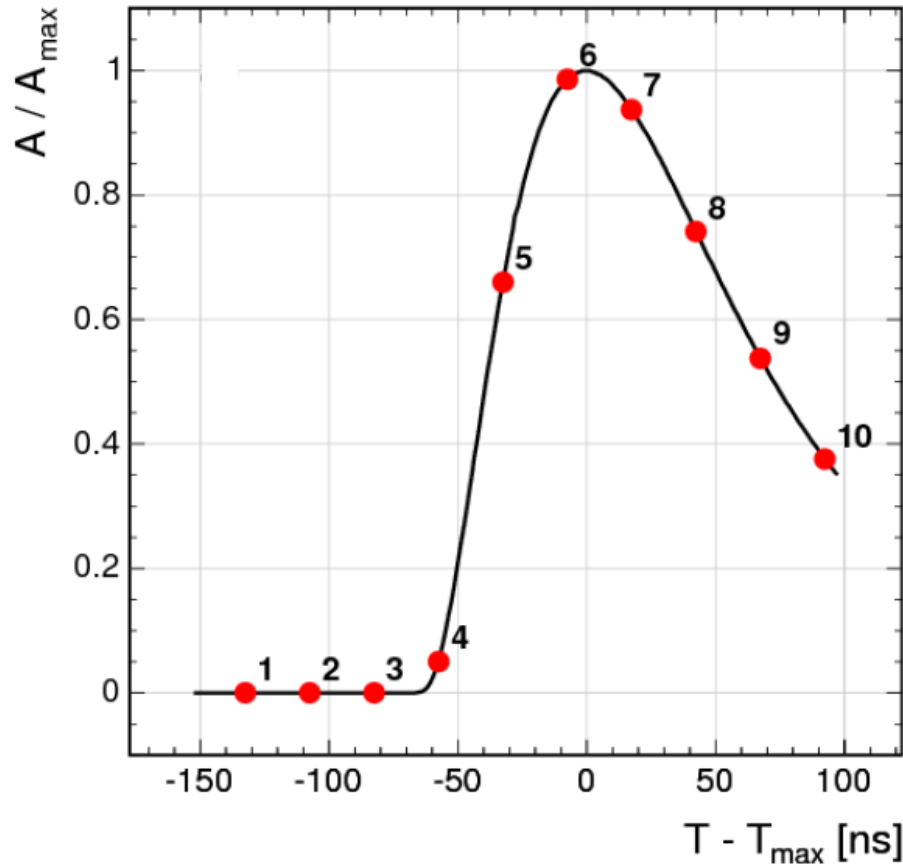


Figure 20: Typical pulse shape measured in CMS (Extracted from [45]).

4 Energy Estimation for TMDB

Reconstruction energy methods in modern calorimeters usually provide the signal detection by performing the amplitude estimation of the signal of interest. The goal of this chapter is to present the energy estimation method proposed for the TMDB: the matched filter (MF), proposed in [46] for TileCal. The method is derived from the matched filter for signal detection [29].

4.1 Signal Detection

The purpose of a detection system is to detect, with maximum efficiency, the presence of a signal transmitted through a channel that introduces an additive noise. Therefore, the system performance should optimize the decision among 4 hypothesis, labeled at Table 1.

Table 1: Four possible states for a detector.

	Response "Absent"	Response "Present"
Signal Present	Miss	Hit
Signal Absent	Correct Rejection	False Alarm

Consider a given discrete signal $g[k]$ and an additive noise $n[k]$, where k represents the samples. The detection problem can be described as a function of the received signal as follows:

$$H_0 : r[k] = n[k] \quad k = 1, 2, \dots, N \quad (4.1)$$

if the signal is absent (H_0) and

$$H_1 : r[k] = g[k] + n[k] \quad k = 1, 2, \dots, N \quad (4.2)$$

if the signal is present (H_1) [47]. The relationship that maximizes detection efficiency is given by the maximum likelihood ratio [48], as follows:

$$L(r) = \frac{f_{R|H_1}(y|H_1)}{f_{R|H_0}(y|H_0)} \stackrel{H_1}{\gtrless}_{H_0} \gamma, \quad (4.3)$$

where the array \mathbf{r} represents the sequence $r[k]$ and \mathbf{R} is a given outcome at the receiver. The terms $f_{R|H_1}$ and $f_{R|H_0}$ are the probability density functions of the received signal R , given that H_0 and H_1 occurred and γ denotes the detection threshold. Usually, the probability density functions are unknown for the majority of the real detection problems, thus the detection algorithm is designed to estimate $f_{R|H_1}$ and $f_{R|H_0}$ from a development dataset where each event is known in advance.

The detection system performs in favor of the hypothesis with greater probability to minimize the detection error. In other words, if the probability of the received signal given only noise was transmitted is greater than the probability of the received signal given the signal was actually transmitted, the hypothesis H_0 will be chosen and, if the opposite occurs, the system will decide in favor of H_1 .

Notice that the signal amplitude can be introduced in the received signal. In this case, the detection problem can be described as follows:

$$H_0 : r[k] = n[k] \quad k = 1, 2, \dots, N \quad (4.4)$$

$$H_1 : r[k] = Ag[k] + n[k] \quad k = 1, 2, \dots, N \quad (4.5)$$

Therefore, the parameter A is the value to be estimated. When the parameter is described by a random variable with known probability density function, it can be estimated by the Maximum A Posteriori (MAP) estimator [48]. If the same parameter is not a random variable the Maximum Likelihood (ML) [48] estimator should be used.

4.2 The Matched Filter method

In cases where the probability density functions of the noise samples is Gaussian with covariance matrix \mathbf{C} , the maximum likelihood ratio can be described as:

$$L(r) = \frac{\exp\left(-\frac{(r-g)^T \mathbf{C}^{-1} (r-g)}{2}\right)}{\exp\left(-\frac{r^T \mathbf{C}^{-1} r}{2}\right)} \stackrel{H_1}{\gtrless} \stackrel{H_0}{\gtrless} \gamma. \quad (4.6)$$

By performing some algebraic operations on Equation (4.6), the optimum detector is given by [49]:

$$\mathbf{r}^T \mathbf{C}^{-1} \mathbf{g} \stackrel{H_1}{\gtrless} \stackrel{H_0}{\gtrless} \gamma. \quad (4.7)$$

Therefore, the detection procedure optimizes the decision through the inner product between the received signal and a replica of the deterministic signal of interest $\mathbf{g}[k]$ after pre-whitening. In cases where the noise samples are white Gaussian, the covariance matrix \mathbf{C} becomes diagonal and the optimum detector results in:

$$\mathbf{r}^T \mathbf{g} \stackrel{H_1}{\gtrless} \stackrel{H_0}{\gtrless} \gamma. \quad (4.8)$$

In most modern calorimeters, the electronic readout provides a pulse shape of an incoming signal rather similar to the reference pulse shape and the electronic noise

acquired during nominal operation has been shown to be Gaussian. Therefore, the MF approach may achieve good results for this scenario. Optimal TMDB signal detection is performed by using the reference signal pulse shape.

Since the signal pulse shape is represented by seven samples, MF implements a fast finite impulse response (FIR) filter [34] according to Equation (4.7), which is appropriate for online applications.

4.2.1 Amplitude estimation through the matched filter

The acquired TMDB signal can be described as follows:

$$r[k] = ped + n[k] + Ag[k], \quad (4.9)$$

where $r[k]$ is the received signal, $n[k]$ corresponds to the electronic noise, ped is the baseline offset, $g[k]$ is the TMDB reference pulse and A is the amplitude.

The amplitude of the incoming signal can be estimated through the inner product between the received signal and the TMDB reference pulse after pre-whitening. The inner product operation is shown in Equation (4.10):

$$y = (\mathbf{r} - ped)^T \mathbf{C}^{-1} \mathbf{g}. \quad (4.10)$$

Hence, the expression for the estimated amplitude results in:

$$\hat{A} = \frac{(\mathbf{r} - ped)^T \mathbf{C}^{-1} \mathbf{g}}{\mathbf{g}^T \mathbf{C}^{-1} \mathbf{g}}. \quad (4.11)$$

Figure 21 illustrates the signal reconstruction procedure using the Matched Filter.

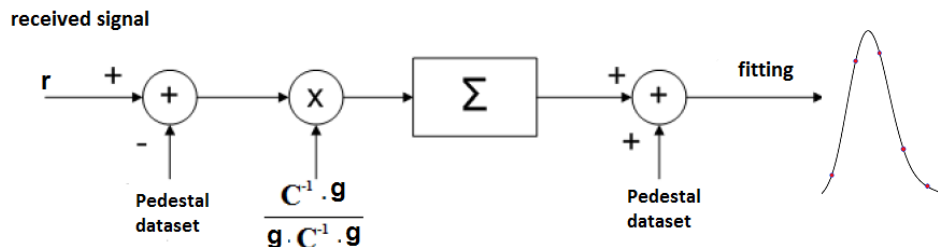


Figure 21: Signal reconstruction procedure using the Matched Filter(Extracted from [46]).

4.2.2 Matched Filter implementation on FPGA

Figure 22 shows the Matched Filter implementation as well as the classical estimation methods discussed in Section 3.3. Notice that the implementation corresponds to

a fast finite impulse response (FIR) filter with N coefficients. Hence, only N multiplications are required to estimate the signal amplitude.

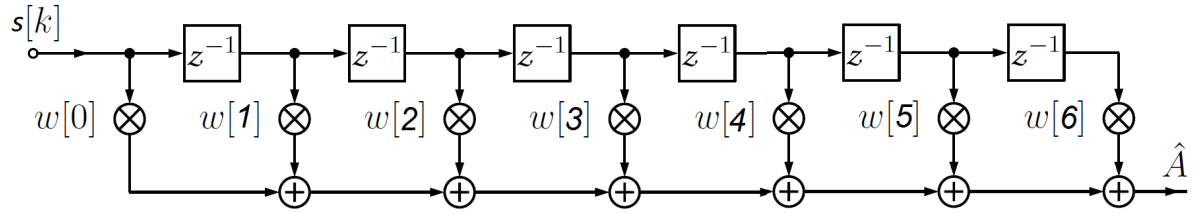


Figure 22: The Matched Filter implementation for $N=7$.

5 TMDB Commissioning Analysis

Sixteen TMDBs were installed and integrated into the Tile Calorimeter data acquisition system, depicted in Figure 23, during the LHC technical stop in 2015. The TileMuon system is now in the commissioning phase, preparing to start operation by the middle of 2017.

The TMDB energy estimation is performed by a 7-coefficient FIR filter that is based on a Matched Filter (MF) approach. The MF coefficients are computed per readout channel using the respective reference pulse-shape and noise covariance matrix. The TMDB output is converted to MeV using calibration parameters computed through a linear fit based on the offline TileCal channel energy in MeV. Therefore, for each channel, the Matched Filter and calibration parameters were designed based on a database acquired by the TMDBs during the 2016 commissioning. Analysis of noise amplitude was also done to evaluated the TMDB performance.

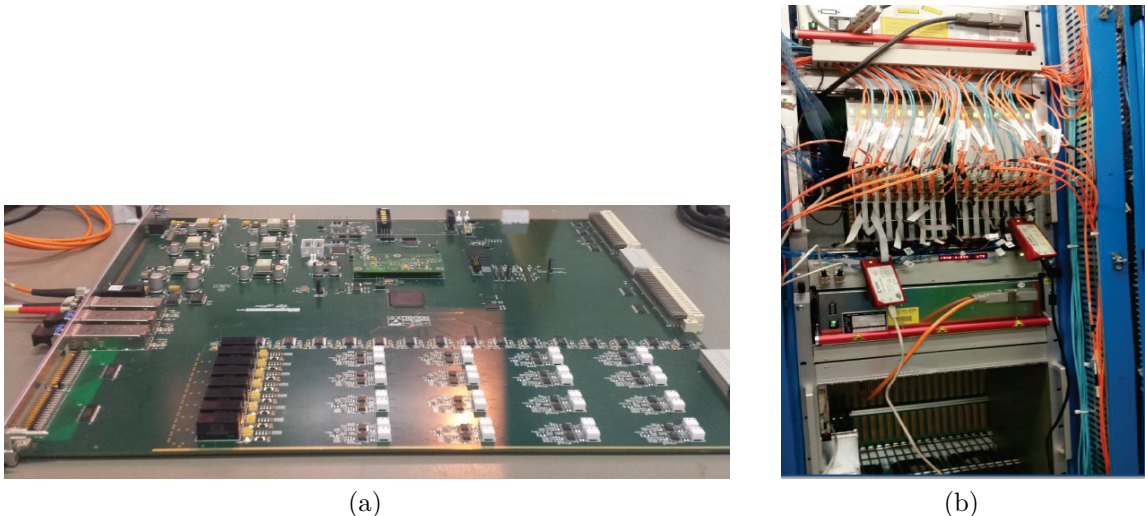


Figure 23: The TMDB hardware system: (a) the TileMuon digitalizer board. (b) the TMDB crate.

5.1 Database

The database used for matched filter design comprises two classes: the noise dataset, which refers to noise acquisition from dedicated standalone runs (often called pedestal runs) and, the signal dataset, which was acquired from proton–proton collisions corresponding to an integrated luminosity of 471.3 pb^{-1} with 40 MHz event rate collected by the ATLAS detector at the LHC at a center-of-mass energy of $\sqrt{s} = 13 \text{ TeV}$ in 2016.

5.2 Noise Characteristics

In order to calculate the matched filter weights, both noise characteristics and the pulse shape must be understood. The noise dataset, used to calculate the noise distribution and the noise autocorrelation matrix, comprises of 3.461 events acquired from each TMDB channel during nominal TileCal operation.

Figure 24 illustrates the noise distribution for four channels from one TileCal module¹. The noise distributions were fitted with Gaussian and compared with it through the likelihood radio test [57]. Although the hypothesis test shows the experimental samples do not include only a Gaussian process, the MF method will likely operate under optimal conditions, concerning the noise requirement.

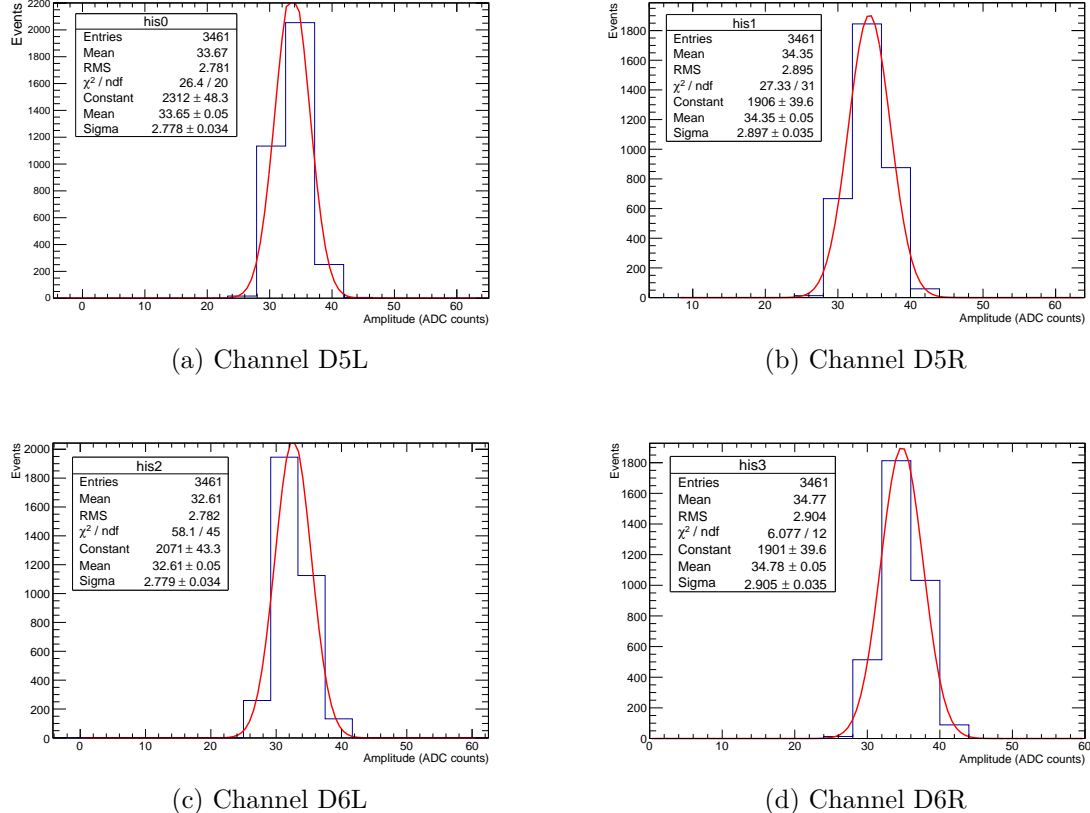


Figure 24: The noise distribution of channels from TileCal module EBA02.

When the noise has correlated Gaussian samples, the performance of the matched filter is affected by the signal shape and the noise covariance matrix has to be considered during the MF design. Figure 25 shows the noise covariance matrix of four channels from one TileCal module, from which one may observe that noise samples are strongly correlated.

¹ Channels D5L, D5R, D6L and D6R of module EBA02

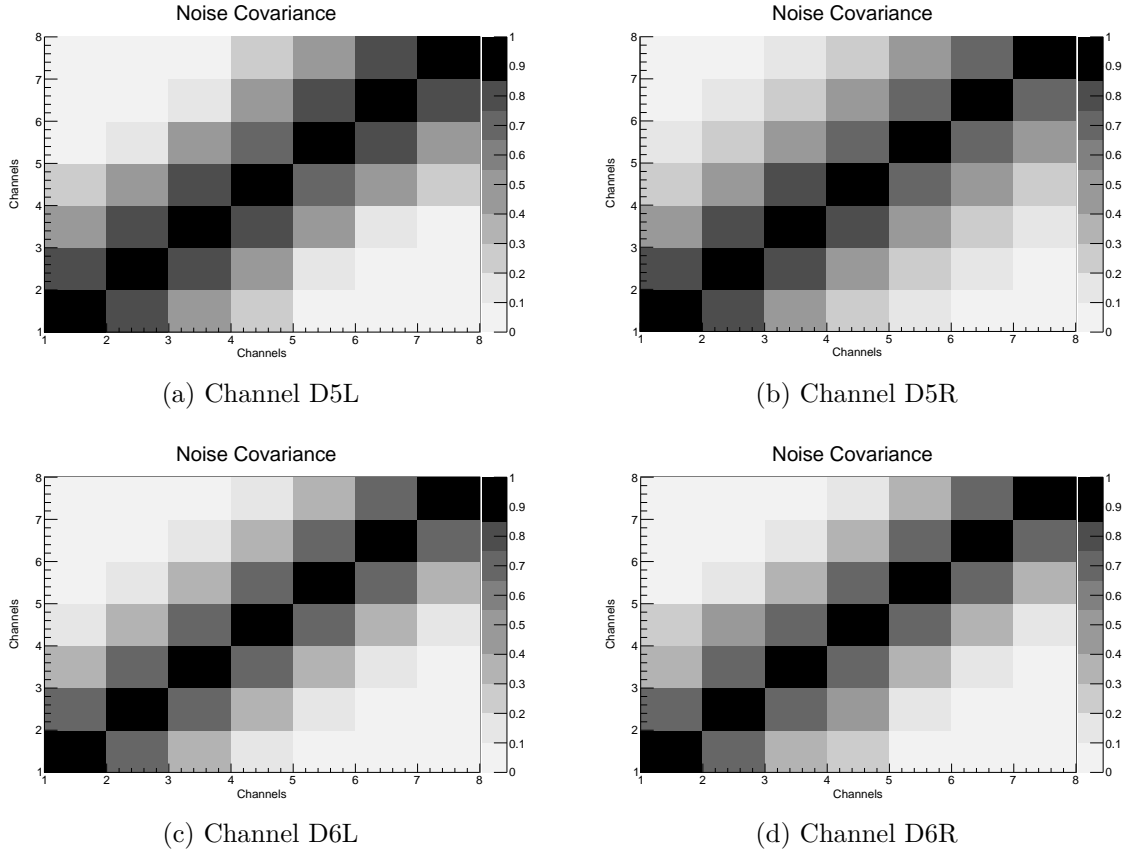


Figure 25: The noise covariance matrix of channels from TileCal module EBA01.

The noise distribution and the noise autocorrelation matrix show similar behaviors as the presented in the Figure 25 for all 512 TMDB channels.

Figures 26 (a) and (c) illustrate the noisy cross correlation between the 256 TMDB channels of a given TileCal side. The same figure were acquired for the 36 channels of one TMDB ², depicted in figures 26 (b) and (d). The elements of the main diagonal were removed in order to emphasize cross-correlations. Notice that the cross correlation between adjacent channels is noticeable for both TileCal sides, with values between 8% and 20%. This result can deteriorate the MF performance, since the noise cross-correlation between the channels are not considered in its design.

² TMDB number TMDB01

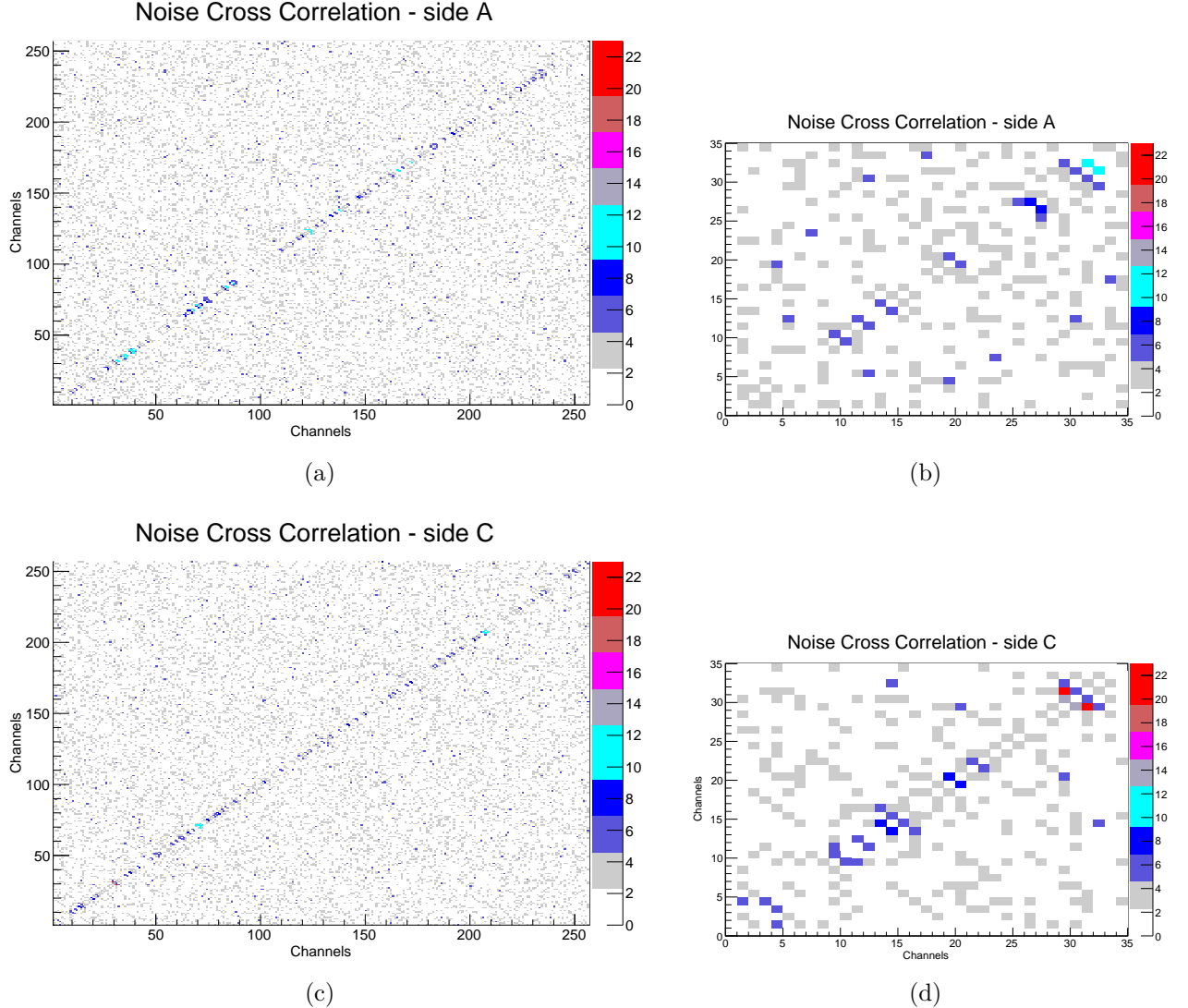


Figure 26: Noise cross correlation between (a) all the channels of A side (b) Channels of one TMDB of A side (c) all the channels of C side (d) Channels of one TMDB of C side.

5.3 Pulse Characteristics

Figure 27 illustrates the averaged TMDB pulse using a proton-proton collision dataset with energy ranging from 1 GeV to 6 GeV (TileCal digital readout). The pulses were acquired for both A and C Tilecal's side. The pulse for each side provides a good representation of the reference pulses acquired per channel used on matched filter design, with agreement greater than 95% when Pearson's chi-squared test (X^2)[58] is applied.

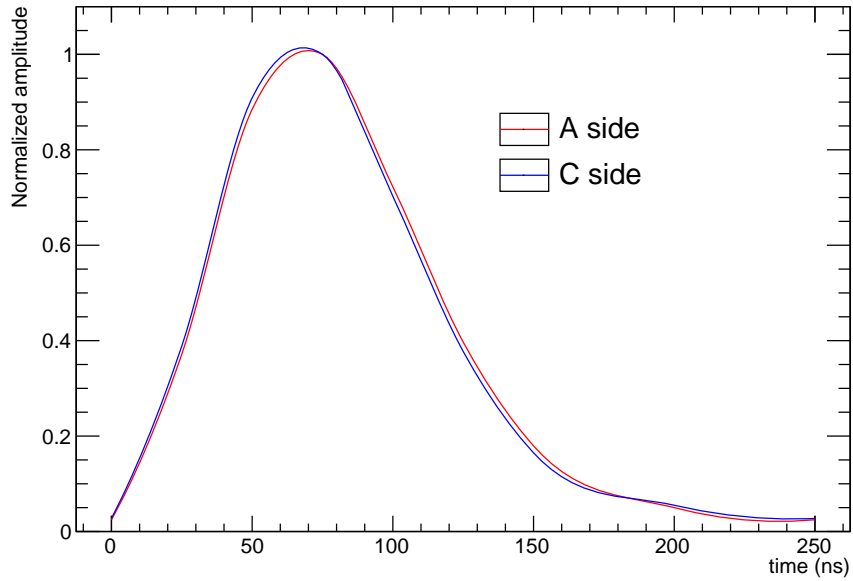


Figure 27: Reference pulse acquired to both A and C Tilecal's side.

5.4 Matched Filter Design

The matched filter weights were calculated for the 512 channels of TMDB and implemented on the system on July 2016. As described in Section 4.2, the design is performed using the reference pulse, and the noise covariance matrix for each readout channel. The reference pulse used in matched filter design is composed by 7 samples of the average pulse of a proton-proton collision dataset with energy ranging from 1 GeV to 6 GeV (TileCal digital readout) acquired for each TMDB channel.

Since the Matched filter requires the pulse shape to provide the signal to noise ratio (SNR) maximization in the presence of additive noise, fluctuations on the pulse shape affects the estimator efficiency. Figure 28 illustrates the pulse shape for 4 different charges (3pC, 6pC, 9pC and 12pC) injected on TileCal by the charge injection system, acquired for one channel of TMDB ³ (interpolated). It can be seen that the pulse shape does not change over the entire dynamic range of the signal.

³ Channel D5L of module EBA01

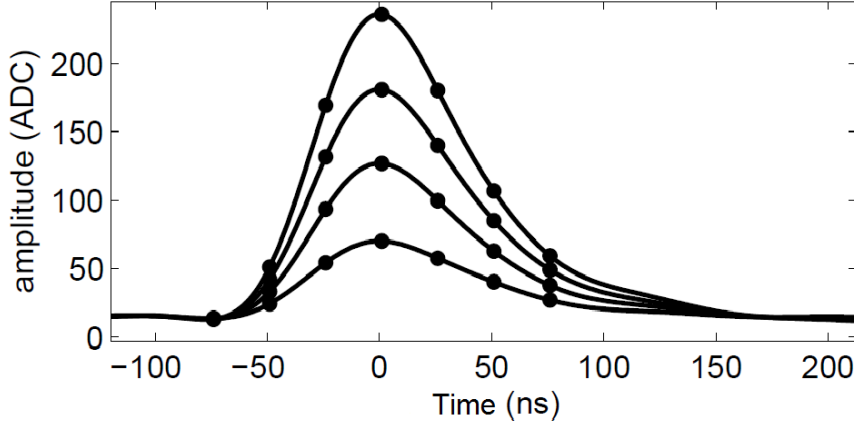


Figure 28: The pulse shape for different charges.

Figure 29 shows the average pulse, acquired for two channels of TMDB, from different proton-proton collisions datasets with energy ranging from 1 GeV to 6 GeV (TileCal digital readout). The pulse shape remains stable and the MF performance is preserved with different datasets for all channels of TMDB.

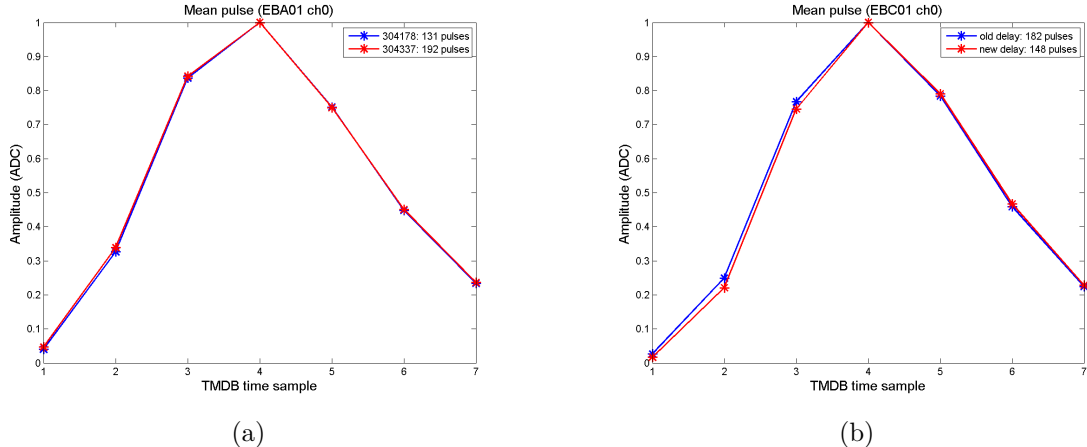


Figure 29: The pulse shape from different proton-proton collisions datasets for (a) channel D5L of TileCal module EBA01 (b) channel D5L of TileCal module EBAC01.

The noise covariance matrix \mathbf{C} was computed using a noise database measured from TMDB during a pedestal run, depicted in Figure 25. Figure 30 illustrates the matched filter weights, calculated as described in Section 4.2, for four TMDB channels⁴.

⁴ Channels D5L, D5R, D6L and D6R of module EBA01

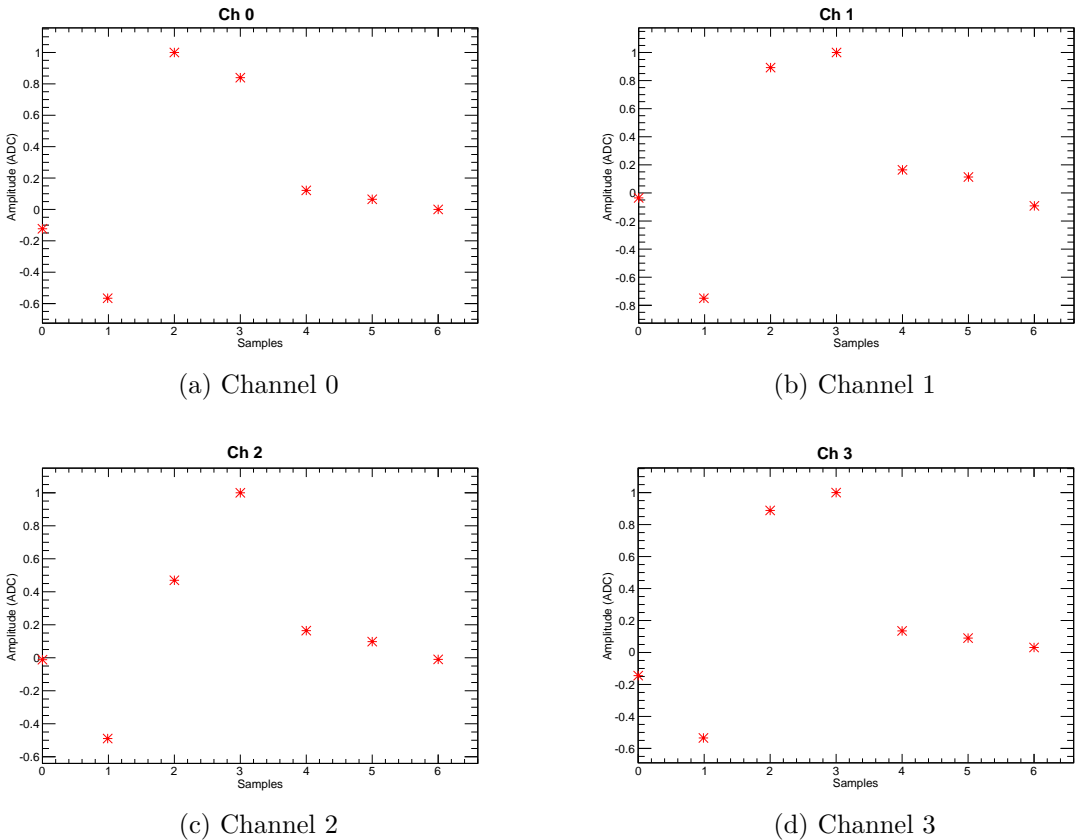


Figure 30: The matched filter weights for channels from TileCal module EBC01.

5.5 Matched Filter Results

The Matched Filter operation provides the TMDB output in ADC counts (in arbitrary units). The energy is converted to mega electron-volt (MeV) using calibration parameters computed through a linear fit based on the TileCal channel energy in MeV reconstructed off-line. Figure 31 illustrates the linear fit computed for one channel of TMDB⁵. The calibration constants were acquired for the 512 channels of TMDB on July 2016.

Figure 32 illustrates the error estimation distribution associated to the MF and calibration operation. The histogram does not show relevant bias (average close to zero) and a RMS of 113.7 MeV is achieved, which is below the original specification of 140 MeV.

5 Channels D5L of module EBC03

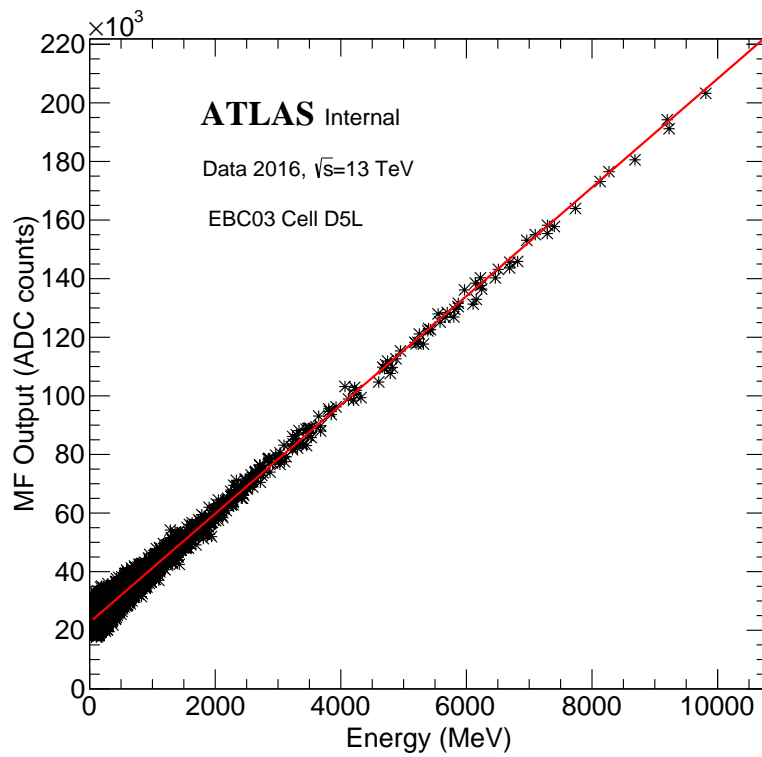


Figure 31: The TMDB calibration output estimated by Matched Filter (arbitrary units) for TileCal module EBC03 channel D5L to convert the value to MeV.

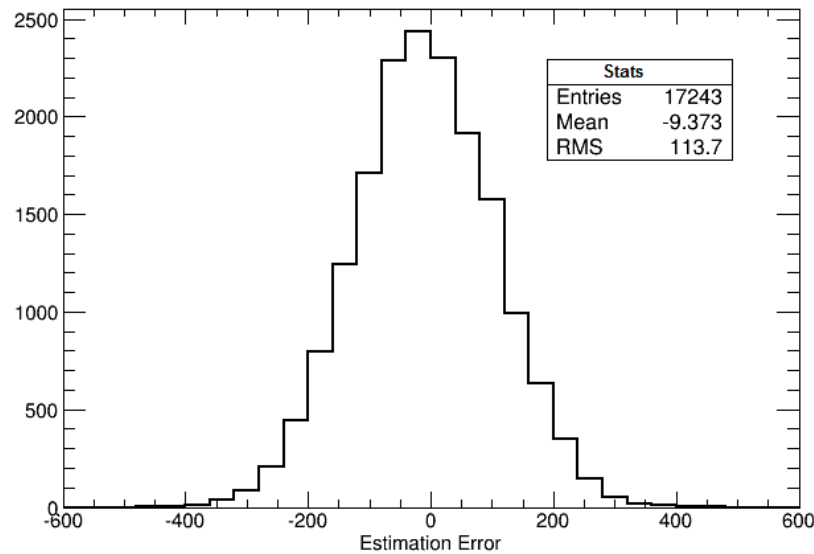


Figure 32: The error estimation distribution for TileCal module EBC03 channel D5L.

The TMDB on-line output, estimated by performing an inner product between the MF coefficients and the incoming time samples in FPGA core, was correlated with the

output provided by off-line operation (i.e applying the MF coefficients on the samples) to verify the on-line MF operation on FPGA. The graph on Figure 33 shows the off-line MF operation along the horizontal-axis and the TMDB on-line output along the vertical-axis for one channel of TMDB⁶. The two variables are linearly correlated, indicating the strongest association between them.

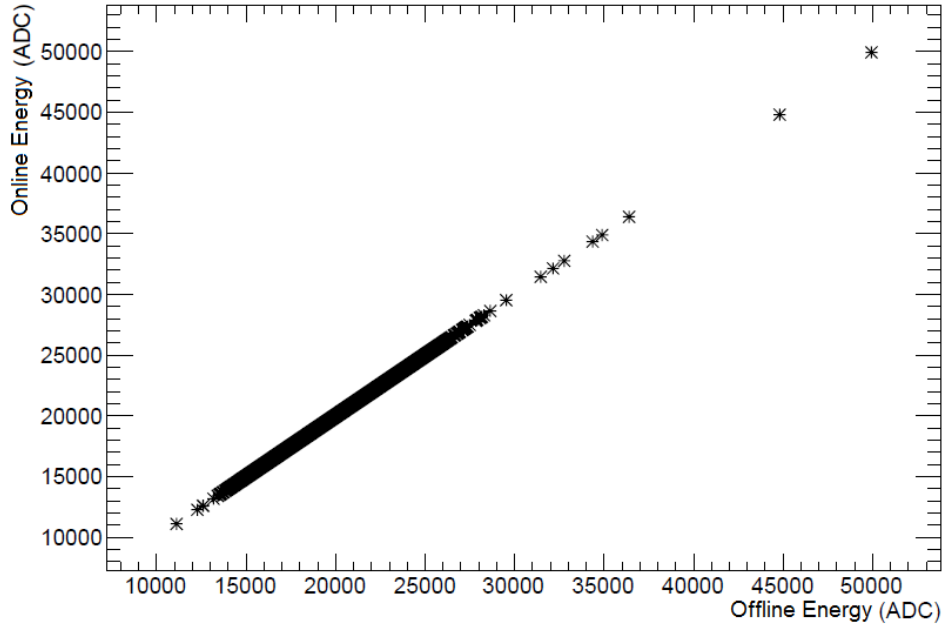


Figure 33: Correlation between the on-line TMDB output (using the variable eTMDB) and the off-line operation.

5.6 System Status

Figure 34 illustrates the noise RMS (in MeV) of each channel using 2016 pedestal data. The global noise measured on the TMDB (105 MeV) is better than the noise predicted on the system proposal (140 MeV). Ten channels (in white) were classified as problematic channels and their coincidence between TGC and TileCal cells are not acquired. They are noisy or dead channels and the problem sources came from the muon signal path before TMDBs (PMTs, front-end electronics, cables). The problematic channels represent 2% of the TMDB channels and they do not affect significantly the system performance.

⁶ Channels D5Lof module EBC03

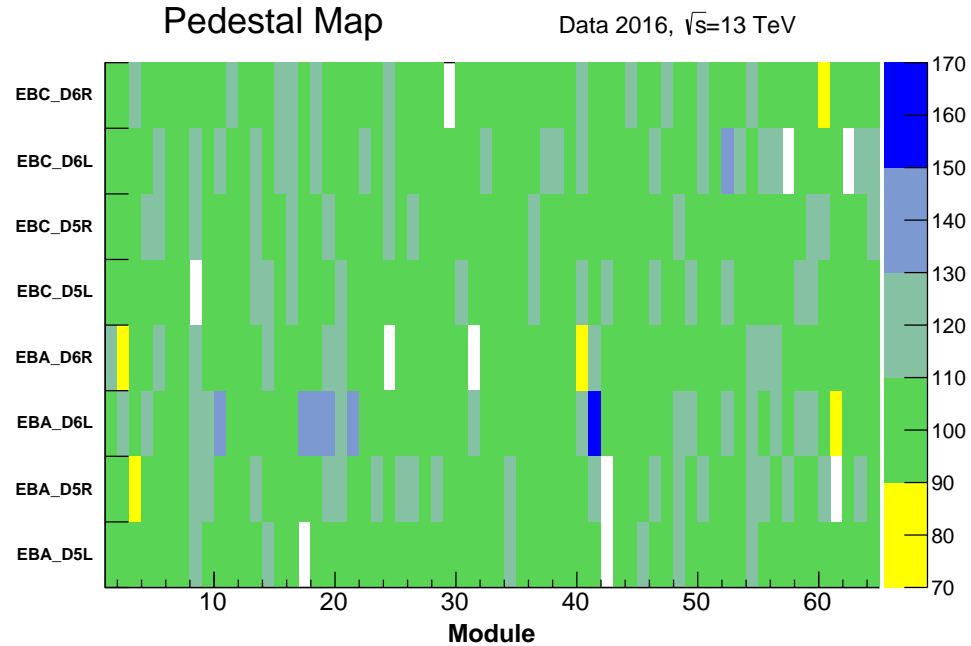


Figure 34: TMDB electronic noise channel map acquired during the pedestal run in 2016.

6 System Performance

The aim of this chapter is to evaluate the TileMuon system performance. Therefore, an analysis of the muon detection efficiency and fake rate reduction has been performed using the whole system: both sides of the TileCal Extended Barrel and the modules of the TileCal Extended Barrel information. The system performance is evaluated through the comparison between the results acquired in this analysis and the system performance specified during system design.

6.1 Muon detection efficiency and fake rate reduction

The TileMuon system provides coincidence between the information of TileCal Extended Barrel (128 TileCal modules divided in A side and C side) and the endcap region composed of 48 trigger sectors for each TileCal Extended Barrel side. For a signal in a muon trigger sector it can be expected that it comes from a high- p_T muon that have also traversed one of the two TileCal modules in front of the Level-1 muon endcap trigger sector.

An analysis has been performed in the region $1 < |\eta| < 1.3$, using data from proton-proton collision at $\sqrt{(s)} = 13$ TeV acquired by TMDB in 2016. The muon events were selected by the TGC trigger ($1 < |\eta| < 1.3, p_T > 20$ GeV) and by offline muon reconstruction ($p_T^{muon} > 15$ GeV). Each muon trigger sector was associated with at least one of the TileCal modules. The efficiency is computed as the ratio between the number of muon events selected with the summed energy deposit in the D5 and D6 cells greater than a pre-determined energy threshold and the total number of muons events selected by the muon trigger. Whereas the fake reduction is provided by the ratio between the number of events rejected by the muon trigger with the summed energy deposit in the D5 and D6 cells greater than a pre-determined energy threshold and the total number of events rejected by the muon trigger. The global muon detection efficiency and the fake reduction of the Level-1 Tile-Muon Trigger, provided by TMDB, as a function of the threshold, are shown in Figure 35.

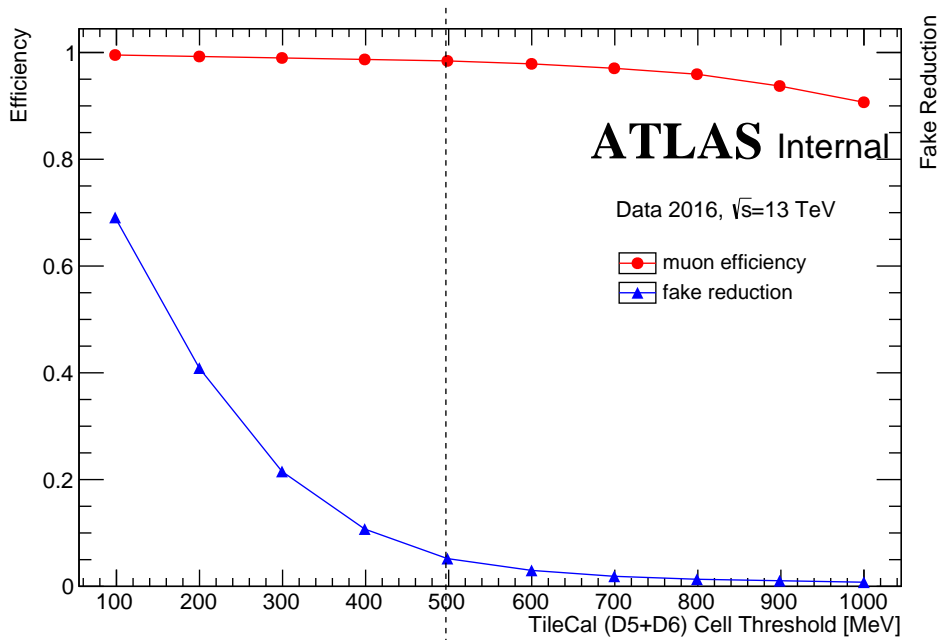


Figure 35: Muon detection efficiency and fake reduction of the Level-1 Tile-Muon Trigger as a function of TileCal cell energy sum threshold.

The coincidence between TileCal and TGC Trigger is performed by software. Using information of D5+D6 TileCal outer radius cells of the Extended Barrel covering $1 < |\eta| < 1.3$ and a threshold cut of 500 MeV, a muon detection efficiency of 98.2% is achieved, while the fake reduction is 3.07%. The result is better than what was achieved by the prototype receiver module, presented in section 2.7, used in 2010-2011 data taking, when 93% of muon detection efficiency and 17% of fake reduction were achieved. Figure 36 shows the muon detection efficiency and the fake reduction of the Level-1 Tile-Muon Trigger as a function of the threshold for each TileCal Extended Barrel side (A side and C side).

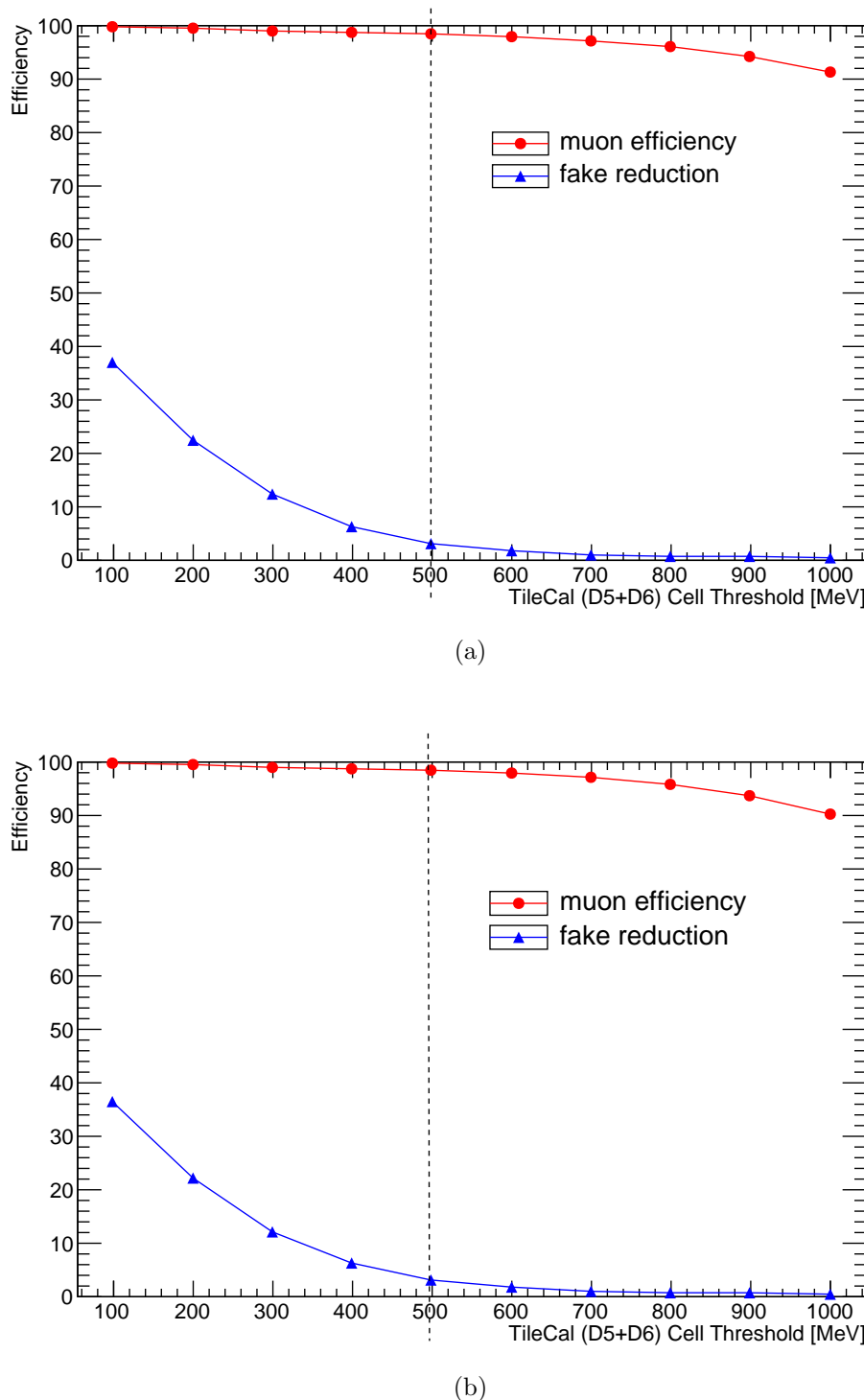


Figure 36: Muon detection efficiency and fake reduction of the Level-1 Tile-Muon Trigger as a function of TileCal cell energy sum threshold (a) A side (b) C side.

The muon detection and the fake reduction curves present similar results for both sides. Using information of D5+D6 TileCal outer radius cells of the Extended Barrel covering $1 < |\eta| < 1.3$ and a threshold cut of 500 MeV, muon detection efficiencies of 98.28% for A side and 98.25% for C side are achieved, while the fake reductions are 3.10%

and 3.02% respectively.

The muon detection and the fake reduction per each module were also evaluated. Figure 37 shows the results for a module with performance better than the average (module EBC25). Its provides a muon detection efficiency of 98.88% and a fake reduction of 2.06%. Whereas Figure 38 illustrates the results for a module with worse than average performance (Module EBA43). In this module a muon detection efficiency of 95.64% and a fake reduction of 6.72% are achieved.

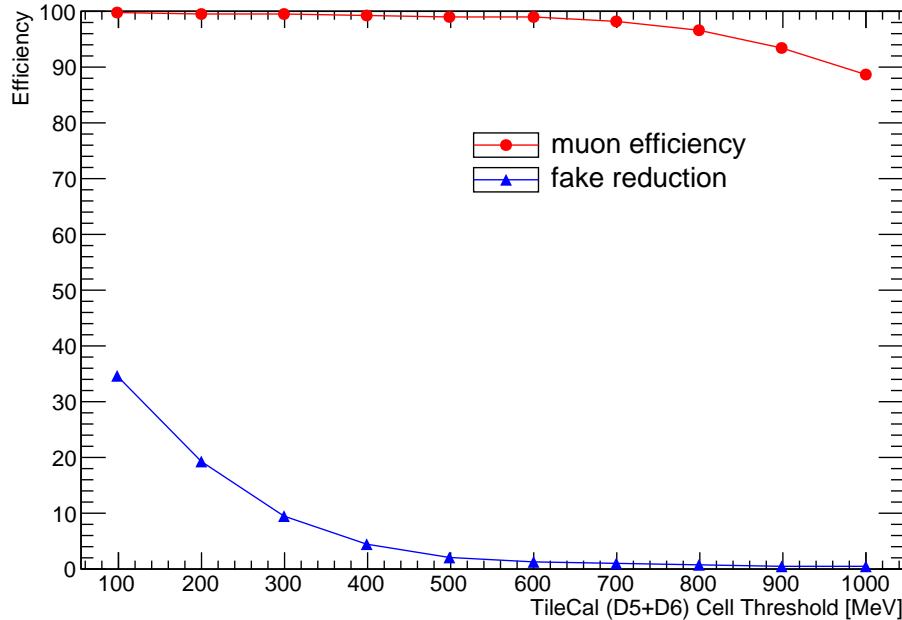


Figure 37: Muon detection efficiency and fake reduction of the Level-1 Tile-Muon Trigger as a function of TileCal cell energy sum threshold for module EBC25.

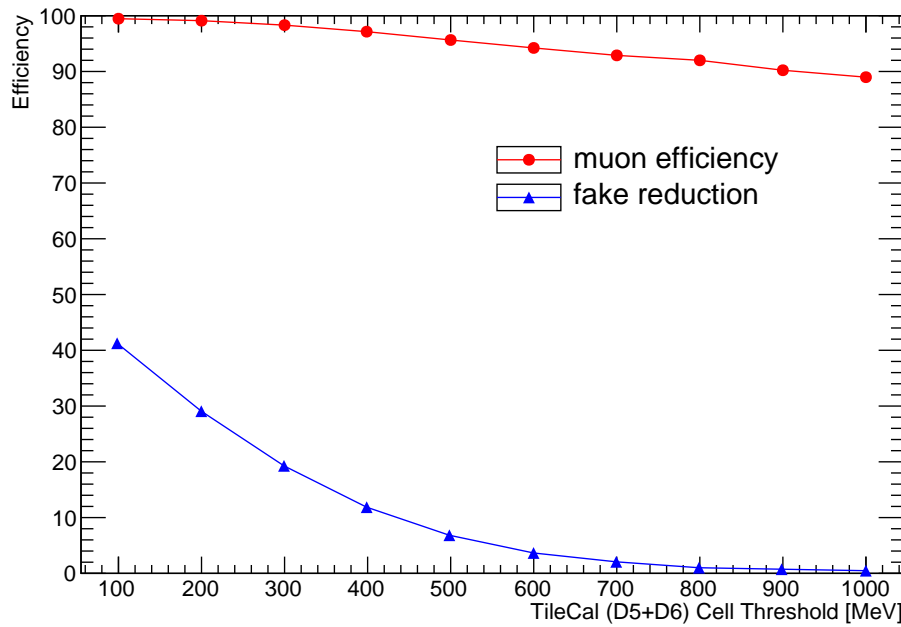


Figure 38: Muon detection efficiency and fake reduction of the Level-1 Tile-Muon Trigger as a function of TileCal cell energy sum threshold for module EBA43.

The measured muon efficiency detection and fake reduction results presented in this chapter shows that the system provides better results than originally proposed (presented in section 2.7).

7 Conclusions

The LHC is currently being upgraded to produce collisions at the centre-of-mass energy near 14 TeV. Therefore, ATLAS has been modified to meet the challenges of new Run 3, when the LHC resumes operation in 2020 after the second long shutdown. The TileCal main activity for the ATLAS upgrade, during Phase 0, was related to the activation of the TileCal outermost D-layer signal for assisting the Level-1 Muon Trigger at $1.0 < |\eta| < 1.3$. In order to receive and process the TileCal muon trigger signals in the extended barrel region, the Tile Muon Digitizer Board was designed, fully tested and produced. Sixteen TMDBs have been installed in the ATLAS cavern and integrated with the Tile Calorimeter. The Tile-Muon system is now in final stage of commissioning phase and ready to be included in ATLAS Level-1 Trigger.

In this dissertation, the TMDB operation performance during the commissioning phase was evaluated. The analysis uses data from proton-proton collision at a center-of-mass energy of 13 TeV and noise from pedestal runs during nominal TileCal operation collected by the TMDB in 2016. The averaged pulses used for the matched filter design provides a good representation of the pulse shape for each channel and remains stable for different proton-proton collisions datasets. A hypothesis test showed that the noise distribution in the TMDB channels do not include only a Gaussian process. A noticeable noise cross correlation between adjacent channels was observed, which compromises the MF optimal performance. It was also noted that the online MF implemented on FPGA is operating as expected.

The proposed method for TMDB signal detection and amplitude estimation was presented and its performance using a simulated and experimental database were compared with an ANN for energy estimation and another one for signal detection. A feed-forward neural network can approximate the Maximum likelihood, whereas the MF performance can be compromised by the restrictions imposed on its design. On other hand, since the MF method implements a FIR filter, it could be simply implemented in the TMDB FPGA whereas the ANN implementation requires more computational effort. Their performance were evaluated through a ROC constructed for each scenario. As the ANN performance was similar to the MF one, it indicates that the MF is operating near optimal conditions.

Analysis of the muon detection efficiency and fake rate reduction were performed using the whole system and compared with the system performance results specified during system design. The Analysis showed that the TileMuon system performance is beyond the predicted one.

Concerning future studies, the TMDB operation performance should be evaluated in the next stage, when the system is included in ATLAS Level-1 trigger. Also, studies of estimation techniques which take in account the noise cross-correlation on its design should be performed.

REFERENCES

- [1] ATLAS Collaboration, “New small wheel technical design report”, CERN-LHCC-2013-006, ATLAS-TDR-020 (2013).
- [2] M. Barnier, M. Calmy-Rey, H.Curien, et al, “Infinitely CERN: memories of fifty years of research”, *Sciences et histoire* (2004).
- [3] L. Evans, P. Bryant, “LHC Machine”, *Journal of Instrumentation* **3** (2008) S08001.
- [4] CERN Collaboration, “The CERN accelerator complex”, OPEN-PHO-ACCEL-2013-056 (2013).
- [5] CERN Collaboration, “CERN Document Server”, 40525 (2008).
- [6] ATLAS Collaboration, “The ATLAS Experiment at the CERN Large Hadron Collider”, *Journal of Instrumentation* **3** (2008) S08003.
- [7] CMS Collaboration, “The CMS experiment at the CERN LHC”, *Journal of Instrumentation* **3** (2008) S08004.
- [8] ALICE Collaboration, “The ALICE experiment at the CERN LHC”, *Journal of Instrumentation* **3** S08002.
- [9] LHCb Collaboration, “The LHCb Detector at the LHC”, *Journal of Instrumentation* **3** S08005.
- [10] W. N. Cottingham, D. A. Greenwood, “An Introduction to the Standard Model of Particle Physics”, *Cambridge University Press* (1998).
- [11] E. Ros, “ATLAS inner detector”, *Nuclear Physics B - Proceedings Supplements* **120** (2003) 337–345, [doi:10.1016/S0920-5632\(03\)01908-X](https://doi.org/10.1016/S0920-5632(03)01908-X).
- [12] ATLAS Collaboration, “Calorimeter Performance Technical Design Report”, CERN/LHCC/96-40 (1997).
- [13] S. Palestini, “The Muon Spectrometer of the ATLAS Experiment”, *Nuclear Physics B* **125** (2003) 337–345, [doi:10.1016/S0920-5632\(03\)91013-9](https://doi.org/10.1016/S0920-5632(03)91013-9).
- [14] CERN Collaboration, “Computer generated image of the whole ATLAS detector”, CERN-GE-0803012 (2008).
- [15] CERN Collaboration, “Computer generated image of the ATLAS calorimeter”, CERN-GE-0803015 (2008).
- [16] R. Wigmans, “Calorimetry - Energy Measurement in Particle Physics”, *Oxford University Press* (2000).

- [17] C. W. Fabjan, “Techniques and Concepts of High-Energy Physics III”, *Springer US* (1985).
- [18] C. Grupen, I. Buvat, “Handbook of Particle Detection and Imaging”, *Springer US* (2012).
- [19] P. Perrodo, “The ATLAS liquid argon calorimetry system”, *Proceedings of ICHEP* (2002).
- [20] TileCal Collaboration, “ATLAS Tile Calorimeter Technical Design Report”, CERN/LHCC/96-42 (1996).
- [21] A. Cerqueira, “Tile Calorimeter Upgrade Program for the Luminosity Increasing at the LHC”, *International School on High Energy Physics* (2015).
- [22] A. Cerqueira, “ATLAS Tile Calorimeter Readout Electronics Upgrade Program for the High Luminosity LHC”, *Proceedings of LISHEP* (2013)
- [23] K. Anderson, et al, “Design of the front-end analog electronics for the ATLAS Tile Calorimeter”, *Nucl. Instrum. Meth.* **551** (2005) 469-476, doi: [10.1016/j.nima.2005.06.048](https://doi.org/10.1016/j.nima.2005.06.048).
- [24] S. Viret, “LASER monitoring system for the ATLAS Tile Calorimeter”, *Nucl. Instrum. Meth.* **617** (2010) 120-122, doi: [10.1016/j.nima.2009.09.133](https://doi.org/10.1016/j.nima.2009.09.133).
- [25] E. Starchenko, “Cesium Monitoring System for ATLAS Tile Hadron Calorimeter”, *Nucl. Instrum. Meth.* **A494** (2002) 381-384, doi:[10.1016/S0168-9002\(02\)01507-3](https://doi.org/10.1016/S0168-9002(02)01507-3).
- [26] ATLAS Collaboration, “ATLAS TDAQ System”, CERN-LHC-2013-018, ATLAS-TDR-023-2013 (2013).
- [27] AT. Kawamoto, S. Vlachos, L. Pontecorvo, J. Dubbert, G. Mikenberg, P. Iengo, C. Dallapiccola, C. Amelung, L. Levinson, R. Richter, and D. Lellouch, “New Small Wheel Technical Design Report”, CERN-LHCC-2013-006, ATLAS-TDR-020 (2013).
- [28] ATLAS Collaboration, “Technical design report for the phase-I upgrade of the ATLAS TDAQ system”, CERN-LHCC-2013-018, ATLAS-TDR-023 (2013).
- [29] S. Kay, “Fundamentals of Statistical Signal Processing: Estimation Theory”, *Pearson* (1993).
- [30] S. Theodoridis, “Machine Learning: A Bayesian and Optimization Perspective”, *Academic press* (2015).
- [31] W. Cleland, E. Stern, “Signal processing considerations for liquid ionization calorimeters in a high rate environment”, *Nucl. Instr. and Meth. in Phys. Res. A* **338** (1994) 467-497, doi:[10.1016/0168-9002\(94\)91332-3](https://doi.org/10.1016/0168-9002(94)91332-3).

- [32] E. Fullana, et al., “Digital Signal Reconstruction in the ATLAS Hadronic Tile Calorimeter”, *IEEE Transaction On Nuclear Science* **53** (2006) 2139–2143, doi:[10.1109/TNS.2006.877267](https://doi.org/10.1109/TNS.2006.877267).
- [33] P. Paganini, I. Van Vulpen, “Pulse amplitude reconstruction in the CMS ECAL using the weights method”, CMS NOTE 2004/025 (2004)
- [34] S. K. Mitra, “Digital Signal Processing: A Computer Based Approach”, *McGraw-Hill* (1998).
- [35] ALICE Collaboration, “The ALICE experiment at the CERN LHC”, *Journal of Instrumentation* **3** (2008) S08002.
- [36] A. Caldwell, et al., “Design and Implementation of a High Precision Readout System for the ZEUS Calorimeter”, *Nuclear Instruments and Methods in Physics Research A* **321** (1992) 356–364, doi:[10.1016/0168-9002\(92\)90413-X](https://doi.org/10.1016/0168-9002(92)90413-X).
- [37] V. Abazov, et al., “The Upgraded D0 Detector”, *Nuclear Instruments and Methods in Physics Research A* **565** (2006) 463–537, doi: [10.1016/j.nima.2006.05.248](https://doi.org/10.1016/j.nima.2006.05.248).
- [38] M. Tylmad, et al., “Pulse shapes for signal reconstruction in the ATLAS Tile Calorimeter”, *Proc. 16th IEEE-NPSS Real Time Conference RT'09* (2009).
- [39] G. Bertuccio, E. Gatti, M. Sapietro, “Sampling and optimum data processing of detector signals”, *Nuclear Instruments and Methods in Physics Research A* **322** (1992) 271-279, doi:[10.1016/0168-9002\(92\)90040-B](https://doi.org/10.1016/0168-9002(92)90040-B).
- [40] M. Delmastro, et al., “A stand-alone signal reconstruction and calibration algorithm for the ATLAS electromagnetic calorimeter”, *IEEE Nuclear Science Symposium Conference Record* **2** (2003) 1110-1114, doi: [10.1109/NSSMIC.2003.1351886](https://doi.org/10.1109/NSSMIC.2003.1351886).
- [41] E. Fullana, “Digital Signal Reconstruction in the ATLAS Hadronic Tile Calorimeter”, *IEEE Transaction On Nuclear Science* **53** (2006) 2139-2143, doi: [10.1109/TNS.2006.877267](https://doi.org/10.1109/TNS.2006.877267).
- [42] J. Lundberg, “Performance of the ATLAS
rst-level trigger with
rst LHC dat”, *Real Time Conference (RT), 17th IEEE-NPSS* (2010).
- [43] J. M. de Seixas, et al., “The TileCal Energy Reconstruction for LHC Run2 and Future Perspectives”, *LISHEP* (2015)
- [44] CERN Collaboration, “Liquid Argon Calorimeter Public Plots”, (2015).

- [45] S. Chatrchyan, “Time Reconstruction and Performance of the CMS Electromagnetic Calorimeter”, *Journal of Instrumentation* **5** (2010), doi: [10.1088/1748-0221/5/03/T03011](https://doi.org/10.1088/1748-0221/5/03/T03011).
- [46] B. S. M., Peralva, “Reconstrução de Energia para Calorímetros Finamente Segmentados”, *Universidade Federal de Juiz de Fora* (2015).
- [47] K. S. Shammugan, A. Breipohl, “Random Signals - detection, estimation and data analysis”, *Wiley* (2001).
- [48] H. L. V. Trees, “Estimation and Modulation Theory, Part I”, *Wiley* (2001).
- [49] B. S. M., Peralva, “An alternative method for the TileCal signal detection and amplitude estimation”, *Journal of Physics: Conference Series* **368** (2012), doi:[10.1088/1742-6596/368/1/012037](https://doi.org/10.1088/1742-6596/368/1/012037).
- [50] A. Sarajedini, R. Hecht-Nielsen and P. Chau, “Conditional Probability Density Function Estimation with Sigmoidal Neural Networks”, *IEEE Transactions on Neural Networks* **10** (1999) 231-238, doi:[10.1109/72.750544](https://doi.org/10.1109/72.750544).
- [51] S. Theodoridis, K. Koutroumbas, “Pattern Recognition”, *Elsevier* (2009).
- [52] J. O. Katz, “Developing neural network forecasters for trading”, *Technical Analysis of Stocks and Commodities* (1992) 58-70.
- [53] C. C. Klimasauskas, “Applying neural networks, in R. R. Trippi and E. Turban, eds.”, *Neural Networks in Finance and Investing: Using Artificial Intelligence to improve Real World Performance* (1993).
- [54] D. Bailey and D. M. Thompson, “Developing neural network applications”, *AI Expert* (1990) 33-41.
- [55] O. Ersoy, Tutorial at Hawaii International Conference on Systems Sciences, Jan. (1990).
- [56] J. C. Principe, N. R. Euliano, W. C. Lefebvre, “Neural and Adaptive Systems: Fundamentals Through Simulation”, *W. Curt Lefebvre* (1997).
- [57] M. Taboga , “Lectures on Probability Theory and Mathematical Statistics”, *CreateSpace Independent Publishing Platform* (2012).
- [58] W. D. Johnson, R. A. Beyl, J. H. Burton, C. M. Johnson, J. E. Romer, L. Zhang. “Use of Pearson’s Chi-Square for Testing Equality of Percentile Profiles across Multiple Populations”, *Open journal of statistics* **5** (2015) 412-420, doi:[10.4236/ojs.2015.55043](https://doi.org/10.4236/ojs.2015.55043).
- [59] K. S. Shamugan, A. M. Breipohl, “Random Signals detection, estimation and data analysis”, *Wiley* (2001).

APPENDIX A – Scientific Publications

A.1 Work published in congress annals

1. D. Gonçalves, B. S. Peralva, L. M. A. Filho, A. S. Cerqueira, "Estimação da Energia do Sinal de Múons do Calorímetro Hadrônico do Experimento ATLAS", *Simpósio Brasileiro de Telecomunicações (SBrT2015)* (2015).

Abstract: This work presents the study, the development and the implementation of the energy estimation technique in the context of a project related to experimental high energy physics. Estimation techniques found in the literature were applied to the problem and confronted against each other. The results for both simulated and experimental data shown that the pulse amplitude estimator based on the maximum likelihood for Gaussian noise achieved the best performance in terms of estimation error as well as online implementation feasibility, and it has been the chosen technique for the application.